Geotextiles and Geomembranes xxx (xxxx) xxx–xxx

Contents lists available at ScienceDirect

Geotextiles and Geomembranes

journal homepage: www.elsevier.com/locate/geotexmem

Performance of geosynthetic-reinforced soil foundations across a normal fault

Kuo-Hsin Yang[a,*], Jung Chiang[a], Chao-Wei Lai[b], Jie Han[c], Ming-Lang Lin[a]

[a] Department of Civil Engineering, National Taiwan University (NTU), 1, Sec. 4, Roosevelt Rd., Taipei, 106, Taiwan
[b] Department of Civil and Construction Engineering, National Taiwan University of Science and Technology (Taiwan Tech), 43, Sec. 4, Keelung Rd., Taipei, 106, Taiwan
[c] Department of Civil, Environmental and Architectural Engineering, The University of Kansas, 2150 Learned Hall, 1530 W. 15th St., Lawrence, KS, 66045, USA

ARTICLE INFO

Keywords:
Geosynthetics
Geosynthetic-reinforced soil foundation
Normal fault
Differential settlement
Angular distortion

ABSTRACT

This paper presents a series of model tests on geosynthetic-reinforced soil (GRS) foundations across a normal fault. The aim was to evaluate the performance of reinforced foundations as a mitigation measure for surface faulting hazards. Experimental tests modeled a 3-m thick foundation in prototype subjected to a fault displacement up to 90 cm. Test variables included the number of reinforcement layers, reinforcement stiffness and location, and foundation height. Digital image analysis techniques were applied to determine the ground settlement profile, angular distortion, shear rupture propagation, and mobilized reinforcement tensile strain at various magnitudes of fault offset. Test results revealed that compared with the unreinforced foundation, reinforcement inclusion could effectively prevent the shear rupture propagating from the bedrock fault to the ground surface. It also spread the differential settlement to a wider influential zone, resulting in an average reduction of 60% in the fault-induced angular distortion at the ground surface. The maximum angular distortion decreased as the foundation height, number of reinforcement layers, and reinforcement stiffness increased. Relationships between the maximum angular distortion and maximum mobilized reinforcement tensile strain with fault displacement were therefore established. Based on the findings from this study, design suggestions and implications are discussed.

1. Introduction

Surface fault rupture has been recognized as one of the principal earthquake hazards that can cause severe damage to structures and facilities and result in a significant loss of life. Four hazards associated with surface faulting at the ground surface are: 1) distinct shear rupture, 2) significant differential settlement or angular distortion, 3) development of tensile strains in soil, and 4) development of tension cracks (Anastasopoulos et al., 2007; Bray, 2001; Lazarte et al., 1994). To avoid these devastating hazards, construction of buildings with structural foundations that are across or adjacent to the existing surface fault rupture should be avoided. Some laws restrict the construction of buildings within site-specific fault setbacks. If linear infrastructures (such as roads, highways, and tunnels) must cross the areas that may undergo surface fault rupture, structural and geotechnical engineering measures should be implemented to mitigate adverse impacts arising from surface faulting. Structural measures involve constructing post-tensioned or reinforced foundation slabs to accommodate the extra shear stress and bending moment induced by ground deformation. Geotechnical measures involve 1) constructing ductile compacted earth fills, often reinforced with geosynthetics, to partially absorb underlying fault movement and thus reduce angular distortion at the ground surface (Bray, 2001; Bray et al., 1993), or 2) installing special foundations to divert the fault rupture and limit structural distortion (Argyrou et al., 2019; Garcia and Bray, 2019a, 2019b; Ashtiani et al., 2018; Loli et al., 2018; Fadaee et al., 2016; Oettle and Bray, 2013; Anastasopoulos et al., 2009).

Geosynthetics have previously been used to mitigate surface faulting hazards in central Taiwan. In this example, an extension of a highway was constructed in Taichung, Taiwan, with a section planned to cross the Chelungpu fault. This fault had caused significant displacements along the approximately 100-km long surface fault rupture during the 1999 Chi-Chi earthquake (Richter magnitude scale $M_L = 7.3$) (Chen et al., 2001). The highway bureau required the seismic performance of this highway should be functionality (specifically no collapse or significant structural damage) when the next earthquake

* Corresponding author.
E-mail addresses: khyang@ntu.edu.tw (K.-H. Yang), d06521003@ntu.edu.tw (J. Chiang), ak007610005399@gmail.com (C.-W. Lai), jiehan@ku.edu (J. Han), mlin@ntu.edu.tw (M.-L. Lin).

https://doi.org/10.1016/j.geotexmem.2019.12.007
Received 21 August 2019; Received in revised form 6 December 2019; Accepted 10 December 2019

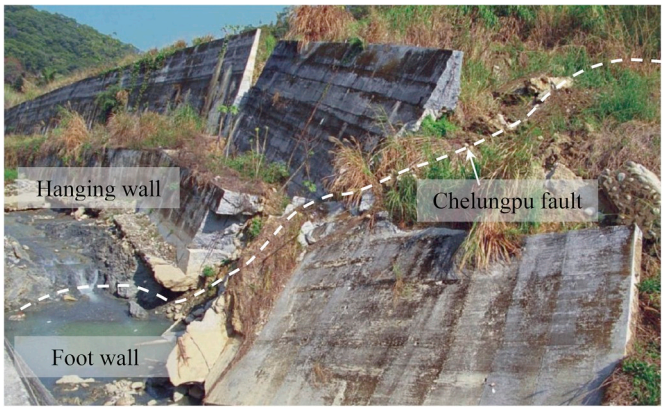

Fig. 1. Collapse of a gravity type retaining wall that straddled an active fault during the Chi-Chi earthquake.

occurs. Previous failure experiences had shown that gravity-type retaining walls were too rigid to withstand large differential settlement induced by fault displacements (Fig. 1). The final decision of this highway extension project was, therefore, to design a ductile highway embankment to traverse the surface fault rupture zone using geosynthetic-reinforced soil (GRS) structures in lieu of conventional concrete retaining walls. The GRS structure consists of a GRS wall and an underlying GRS foundation (Fig. 2). The GRS foundation was adopted to enhance the bearing capacity of the foundation soil and reduce the extent of fault-induced angular distortion to an acceptable level. The GRS wall was constructed to accommodate the differential settlement at the ground surface and maintain the stability and serviceability of the highway embankment. The focus of this study is to investigate the effect of the GRS foundation on reducing the fault-induced angular distortion at the ground surface.

Past studies have investigated the performance of GRS structures subjected to total or differential settlements under circumstances such as saturated soil undergoing consolidation, expansive soil with significant volume changes during wetting and drying cycles, soft soil with high compressibility, landfill liner founded on decomposed waste, heterogeneous soil strata with distinct compressibility, and grounds with voids due to scouring or nearby excavation (Ardah et al., 2018; Sadat et al., 2018; Huang, 2017; Talebi et al., 2017; Chen et al., 2016; Kost et al., 2014; Viswanadham and Konig, 2009; Stulgis et al., 1996; Bergado et al., 1991). Design methods for GRS structures on yielding foundations have been developed for both internal and external stability of GRS walls (Tin et al., 2011; Skinner and Rowe, 2005a, 2005b, 2003). Several past studies have shown the benefits of using geosynthetics to reduce settlements and maintain the system stability and integrity of projects involving landfill liner, bridge abutment, widened embankment, and roadway subgrade (Puppala et al., 2019; Marx and Jacobsz, 2018; Divya et al., 2017; Zheng and Fox, 2017; Miao et al., 2014; Kuwano et al., 2013; Ohta et al., 2013; Jiang et al., 2012; Rajesh and Viswanadham, 2012; Han et al., 2007; Viswanadham and Muthukumaran, 2007; Helwany et al., 2003; Bergado et al., 1991). Studies recognized the main reinforcing mechanism is the tensioned membrane effect, whereby geosynthetics carry the overlying soil by spanning over the yielding foundation and meanwhile mobilizing the tensile forces to minimize the influence from ground settlements (King et al., 2019; Holtz et al., 1998; Giroud et al., 1990).

Although there have been numerous studies on the design and performance of GRS structures on yielding foundations, few have utilized geosynthetics to mitigate surface faulting problems. Bray (2001) and Bray et al. (1993) conducted a series of studies to evaluate the effect of reinforced foundations as a mitigation measure for surface faulting hazards. These comprised simulated earth fills reinforced with 2–4 layers of geogrid subjected to small normal fault movement (up to 5 cm). The numerical results showed that the use of geosynthetic reinforcement or an increase in fill height minimized the angular distortion and soil tensile strain at the ground surface. This measure made it feasible to construct buildings with an acceptable level of risk at the study site. Moosavi and Jafari (2012) conducted both physical and numerical studies to investigate the effectiveness of mitigation of the differential displacement induced by a reverse dip-slip faulting using geosynthetics. They found that using a layer of geogrid in soil foundations can effectively reduce the magnitude of angular distortion at the ground surface. Ohta et al. (2013) proposed a confined-reinforced earth (CRE) technique for asphalt concrete pavements to reduce the risk of earthquake-induced differential settlement damage. The confined-reinforced earth consisted of a geosynthetic-reinforced soil layer restricted by an array of post-tensioning anchors. Full-scale tests of unreinforced (conventional) and CRE pavements underlain by a 2-m high earth embankment were performed. The differential settlement was imposed by using multiple large hydraulic jacks supporting the steel deck placed under the embankment body. The test results showed that the CRE performed acceptably until the force-induced differential settlement reached 55 cm.

As discussed, only a few studies have shown that the use of geosynthetic reinforcement is a valid mitigation measure against surface fault rupture hazards. In particular, the effect of reinforcement

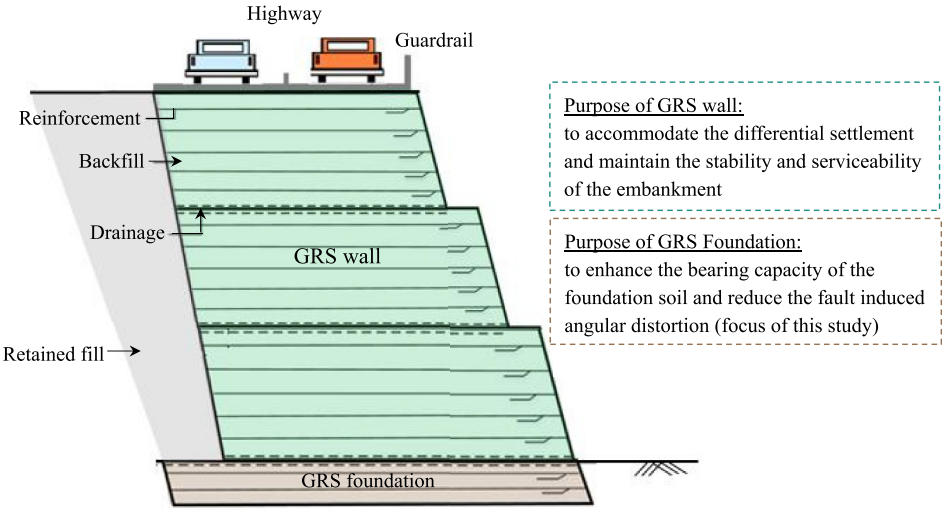

Fig. 2. Schematic illustration of GRS structures constructed in central Taiwan as a highway embankment to mitigate hazards associated with surface fault rupture.

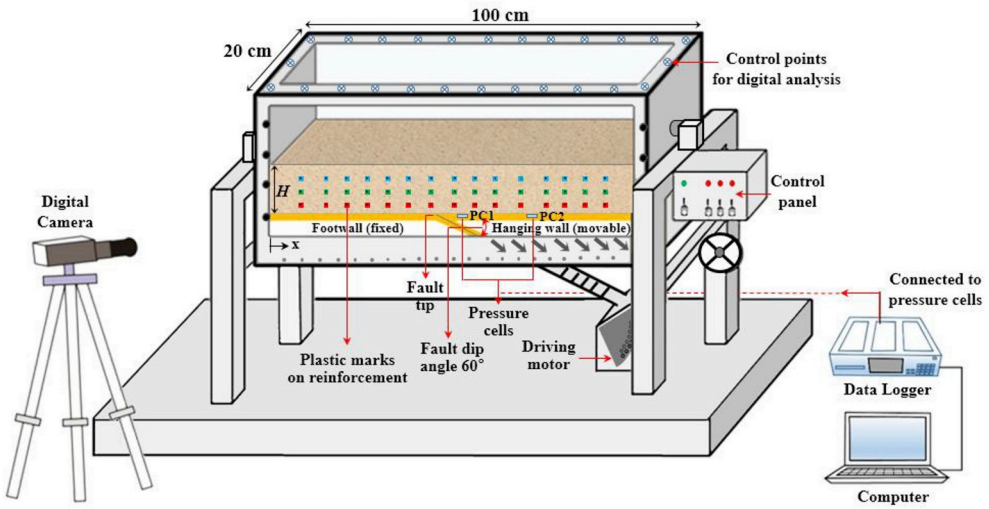

(a)

(b)

Fig. 3. The sandbox and test setup: (a) illustration; (b) panorama.

parameters on the performance of a reinforced foundation subjected to surface faulting has not been fully studied. Furthermore, the mobilized reinforcement tensile force as fault displacement occurs, is important information for the design to prevent reinforcement breakage, but has not been reported in previous studies. The above situations motivated the authors to conduct a series of reduced model tests to investigate the performance of a reinforced foundation underlain by a normal fault. The specific objectives of this study were to 1) compare the surface fault rupture and angular distortion at ground surface of unreinforced and reinforced foundations; 2) evaluate the effect of reinforcement parameters (e.g., layers, stiffness, and locations) and foundation height on the performance of reinforced foundations; 3) examine the relationships of ground angular distortion and mobilized reinforcement tensile force with fault displacement; and 4) provide design suggestions for the use of a reinforced foundation against surface faulting. This paper first introduces the reduced model tests conducted in the present study, and then describes soil and reinforcement materials, model preparation, test procedure, and digital image analysis (DIA) techniques. The test results regarding the ground settlement profile, angular distortion, shear rupture propagation, and mobilized reinforcement tensile strain of reinforced foundations are presented and discussed. Finally, based on the findings, design suggestions and implications are discussed.

2. Reduced model tests

2.1. Reduced model and test program

The reduced model tests on unreinforced and reinforced soil foundations were conducted using a sandbox in the geotechnical research laboratory at National Taiwan University. Fig. 3 presents an illustration and overview image of the sandbox and test setup of the reduced-scale model test. The dimensions of the sandbox were 100 × 20 × 60 cm (length × width × height). Transparent Plexiglas walls were installed on two longitudinal (i.e., front and back) sides of the sandbox for visual observation of soil deformation during the test. To ensure that the soil model was tested under a plane strain condition, a thin plastic sheet

Table 1
Experimental program and test results at the maximum fault offset.

Test variables	Test ID	Test variables			Test results[a]		
		Number of reinforcement layers L	Foundation height H (cm)	Reinforcement stiffness $J_{50\%}$ (kN/m)	Maximum angular distortion β_{max}	Percentage reduction[b] R_d (%)	Maximum mobilized tensile strain ε_{max} (%)
Unreinforced	U	–	20	–	0.72	–	–
Reinforced (Baseline case)	R-3L	3	20	5.5	0.280	61	11.6
Reinforcement location	R-1L-3/4E	1	20	5.5	0.302	58	7.8
	R-1L-1/2E	1	20	5.5	0.320	56	10.7
	R-1L-1/4E	1	20	5.5	0.420	42	12.2
Foundation height	R-3L-10H	3	10	5.5	0.325	55	8.7
	R-3L	3	20	5.5	0.280	61	11.6
	R-3L-30H	3	30	5.5	0.264	63	14.0
Reinforcement stiffness	R-3L	3	20	5.5	0.280	61	11.6
	R-3L-2J	3	20	11.0	0.262	64	7.2
	R-3L-3J	3	20	16.5	0.252	65	5.9
Number of reinforcement layers	R-1L-1/2E	1	20	5.5	0.320	56	10.7
	R-3L	3	20	5.5	0.280	61	11.6
	R-4L	4	20	5.5	0.280	61	10.7
	R-6L	6	20	5.5	0.280	61	9

[a] test results at $S = 6$ cm;
[b] compared to the β_{max} of the unreinforced foundation.

with lubricant was applied at the internal face of each Plexiglas wall to minimize side friction at the soil–wall interface. The bottom of the sandbox consisted of a movable hanging wall and a fixed footwall. Normal or reverse fault displacement was generated by moving the hanging wall upward or downward by using a driving motor installed underneath the sandbox. This study focuses on the test results of a foundation model subjected to normal fault displacement. The initial location of the tip of the bedrock fault was $x = 54$ cm from the left boundary. The fault dip angle was set to be 60° in the present study.

Table 1 summarizes the experimental test program and the corresponding variables. A total of 11 reduced model tests were conducted. Tests U and R-3L (the first two tests in Table 1) were conducted to compare the performance of unreinforced and reinforced foundations under surface faulting. First, the mechanical behavior and effectiveness of reinforcement inclusion on surface faulting mitigation were investigated. The remaining tests in Table 1 were for a parametric study evaluating the effect of reinforcement parameters (i.e., the number of reinforcement layer, reinforcement stiffness, and location) and foundation height on the performance of reinforced foundations subjected to fault displacement. The tests were numbered according to the following rules. The first letter U or R denotes an unreinforced or reinforced model, respectively. The second letter used for reinforced foundations denotes the number of reinforcement layers. The third letter, if any, represents the test variable in the parametric study that differs from the baseline case (Test R-3L). For example, Test R-3L-30H indicates a reinforced foundation with three layers of reinforcement and 30-cm thick foundation. Test R-1L-3/4E indicates a reinforced foundation with one reinforcement layer located at three-quarters of the foundation height (or elevation).

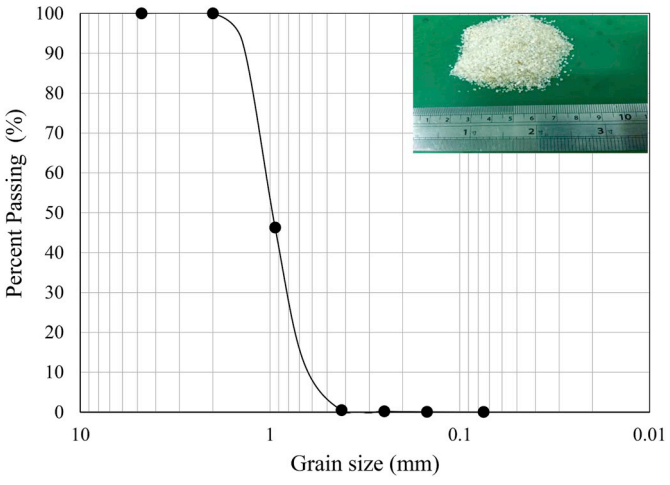

Fig. 4. Grain size distribution curve and photo of the test sand.

2.2. Material properties

The soil used in the tests was uniform quartz sand, which is classified as poorly graded sand (SP) according to the Unified Soil Classification System (USCS). Fig. 4 shows the image and grain size distribution curve of the test sand. Table 2 summarizes soil properties, which were determined in line with ASTM standards. The sand had a specific gravity $G_s = 2.65$, mean particle size $D_{50} = 0.98$ mm, minimum dry unit weight $\gamma_{d,\,min} = 13.5$ kN/m^3, and maximum dry unit weight $\gamma_{d,\,min} = 16.4$ kN/m^3. The corresponding soil unit weight was

Table 2
Soil and reinforcement properties.

Properties	Value
Soil	
Soil classification (USCS)	SP
Specific gravity, G_s	2.65
Mean grain size, D_{50}	0.98
Min. dry unit weight, $\gamma_{d,min}$ (kN/m^3)	13.5
Max. dry unit weight, $\gamma_{d,max}$ (kN/m^3)	16.4
Relative density, D_r (%)	70
Target dry unit weight, γ_d (kN/m^3)	15.3
Cohesion, c' (kPa)	0
Peak friction angle, φ' (°)	39.2
Reinforcement	
Type	Nonwoven geotextile
Material	Polypropylene (PP)
Mass per unit area (g/m^2)	29.60
Thickness (mm)	0.235
Ultimate tensile strength, T_{ult} (kN/m)	0.70
Ultimate tensile strain, ε_{ult} (%)	32.4
Stiffness, $J_{50\%}$ (kN/m)	5.47
Soil-Reinforcement Interface	
Peak interface friction angle, δ '(°)	27.4
Efficiency factor, E_φ	0.63

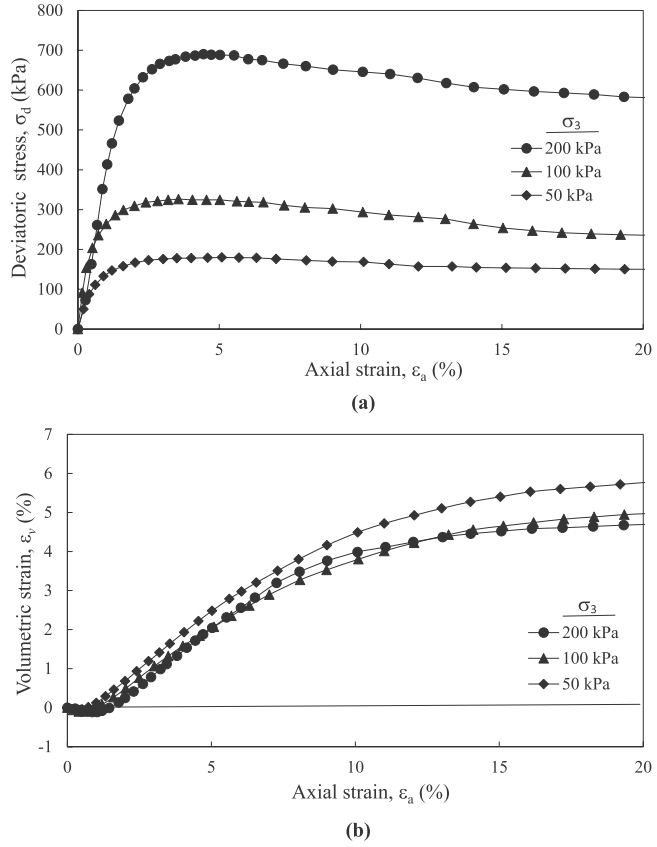

Fig. 5. Triaxial consolidated-drained test results of the test sand: (a)deviatoric stress vs. axial strain; (b) volumetric strain vs. axial strain.

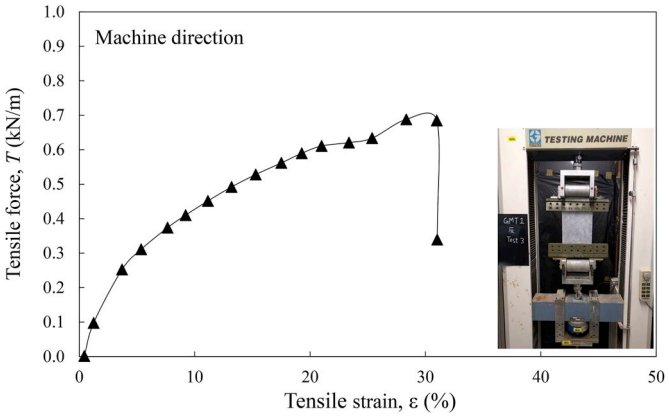

Fig. 6. Wide-width tensile test result of the nonwoven geotextile.

Table 3
Scaling factors and values based on the similarity requirements.

Parameters	[a] Scaling factor	Model	Prototype
Geometry			
Foundation height, H (m)	$1/N$	0.2	3.0
Soil parameter			
Target dry unit weight, γ_d (kN/m^3)	1	15.3	15.3
Friction angle, φ′ (°)	1	39.2	39.2
Reinforcement parameter			
Ultimate tensile strength, T_{ult} (kN/m)	$1/N^2$	0.70	157.5
Stiffness, $J_{50\%}$ (kN/m)	$1/N^2$	5.47	1231
Interface parameter			
Soil-geosynthetic friction angle, δ′ (°)	1	27.4	27.4

[a] Target scaling factor N = 15.

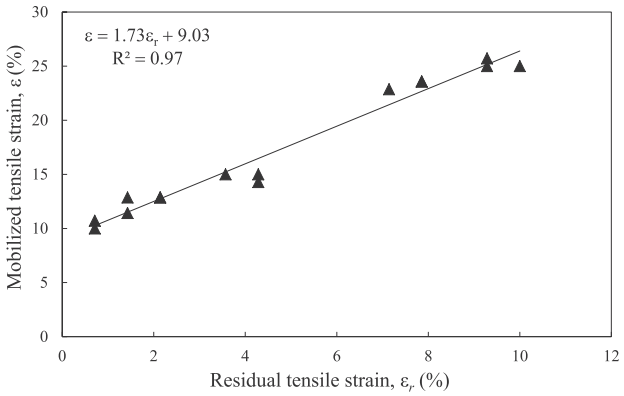

Fig. 7. Correlation between geotextile tensile strain and residual tensile strain.

γ = 15.3 kN/m^3 at the target relative density D_r = 70%. The soil effective cohesion and peak friction angle obtained from consolidated-drained triaxial compression tests were c' = 0 kN/m^2 and φ' = 39.2°, respectively. Fig. 5 shows the measured stress–strain-volumetric strain curves of sand from triaxial CD tests. In addition to shear strength parameters, the soil ductility, expressed as the axial strain at failure, is a controlling factor for the development of a surface fault rupture in boundary deformation problems (Bray, 2001; Bray et al., 1994). As shown in Fig. 5, the measured failure strain of the sand ranged from 2% to 5% for confining pressures σ_3 = 50–200 kPa. In addition, a strain softening behavior was observed for the stress-strain curve under a high confining pressure. Consequently, the sand prepared at the target density showed a relatively brittle behavior.

The reinforcement material used in tests was nonwoven polypropylene geotextile. Table 2 summarizes the properties of this material. Wide-width tensile tests (ASTM D4595) were performed to evaluate the tensile strength properties of the nonwoven geotextile. Fig. 6 shows the results for the nonwoven geotextile tested in the machine direction. The ultimate tensile strength and failure strain were T_{ult} = 0.7 kN/m and ε_f = 32.4%, respectively. The stiffness at the stress level equal to 50% the ultimate tensile strength was $J_{50\%}$ = 5.47 kN/m. The sand-geotextile peak interface friction angle was δ′ = 27.4°, as determined by the interface direct shear test, and the efficiency factor or interaction coefficient was calculated as E = tanδ′/tanφ′ = 0.63. A test geotextile with a low tensile strength was selected with the intention of fulfilling similitude requirements for the reduced-scale model test. Based on the similitude laws for the 1g model tests, the reinforcement tensile strength and stiffness needed to be scaled down to $1/N^2$ of prototype tensile properties (Viswanadham and Konig, 2004). Table 3 lists scaling factors and corresponding values in the prototype for the model geometry and material parameters in the present study.

Nguyen et al. (2013) proposed a technique to derive the mobilized reinforcement tensile strain from the residual tensile strain. This technique was adopted in this study to obtain the maximum reinforcement tensile strains developed at the final fault displacement (i.e., S = 6 cm). The maximum strain values were also used to verify the strain values estimated from the DIA technique (to be discussed later). In this study, mobilized and residual tensile strain relationships were established from a series of wide-width tensile tests by first loading the reinforcement to several target tensile strain levels and then releasing tensile loads. Both target tensile strain values (controlled during tests) and the corresponding residual strain values (obtained after releasing the load) were recorded and plotted. Fig. 7 shows a linear relationship between the mobilized and residual tensile strains of the test geotextile. The intercept in the linear function (as shown in Fig. 7) indicates that the geotextile remained elastic as the developed tensile strain decreased to below 9%, and the plastic deformation began to develop when ε > 9%. Notably, in-isolation and in-soil behavior of nonwoven geotextiles could be different. Soil confinement affects the load-strain response of

nonwoven geotextiles by increasing reinforcement tensile strength and stiffness. However, the strain levels are not significantly affected by soil confinement (Yang et al., 2012; Ballegeer and Wu, 1993; Ling et al., 1992; Wu, 1991; Leshchinsky and Field, 1987). Specifically, the strain at failure remains at approximately the same value at all confinement levels.

2.3. Model preparation and test procedure

The foundation model was constructed by first placing a soil layer and then a reinforcement layer. The required weight of dry sand for each soil layer was calculated for the target soil relative density D_r = 70%. The known quantity of sand was carefully pluviated from a hopper with a specified falling height to achieve a state of uniform density. The geotextile was then laid over the placed sand layer, and the two ends of geotextile layers were fixed to the right and left sides of the sandbox to prevent reinforcement pullout during tests. This approach was designed to simulate the condition whereby the reinforcement is embedded long enough in the soil beyond the fault influence zone in the field. Plastic markers were attached to one longitudinal edge of each reinforcement layer at a regular horizontal spacing to monitor the reinforcement deformation within the soil (Fig. 3). Construction processes used for model preparation were repeated until the foundation model reached the desired height (= 20 cm for most of the cases). According to the similitude laws for the 1 g physical model test (Muir Wood, 2004), this foundation height was equivalent to 3 m in prototype for the target scaling factor of N = 15 selected in this study.

After model construction was completed, fault displacement was generated by moving the hanging wall downward at a constant rate. All tests were terminated at the maximum vertical fault displacement of S = 6 cm (30% of the foundation height) due to the limitation of the capacity of the test equipment. Based on similitude laws, model tests simulated a vertical fault displacement up to 90 cm in prototype. For test monitoring, two earth pressure cells (KYOWA PS-05KC) were mounted on the hanging wall to measure the variation in overburden pressures as fault offset developed. These pressure cells, PC1 and PC2, were located at x = 57 and 77 cm from the left boundary, which were 3 and 23 cm away, respectively, from the fault tip (Fig. 3). During the test, two couple-charged device (CCD) cameras, aimed at the front side and top of the sandbox, were used to continuously monitor soil deformation. The recorded photographic data were then analyzed using various DIA techniques (to be described later) to obtain the ground settlement profile, angular distortion, shear rupture propagation, and mobilized reinforcement tensile strain of reinforced foundations at various magnitudes of fault offset. After tests were completed, each reinforcement sheet was carefully retrieved from the dismantled model to determine the residual tensile deformation of the reinforcement. Because the reinforcement was unloaded after each test, the measured residual tensile strain, indicative of reinforcement plastic deformation, was less than its mobilized tensile strain during the test. The measured reinforcement residual tensile strain was then converted to the mobilized reinforcement tensile strain at the final fault displacement by using the linear function (i.e., $\varepsilon = 1.73\varepsilon_r + 9.03$) as shown in Fig. 7.

2.4. Digital image analysis

A 3D digital terrain model (DTM) was reconstructed using the DIA technique to acquire the ground surface profile at various fault displacements. Control points with known coordinates were set around the top premier of the sandbox (Figs. 2 and 8a). During the test, a series of aerial images was taken at various locations above the sandbox (Fig. 8a). Aerial images containing the coordinate information for control points were then analyzed to establish ground surface DTM using Agisoft image analysis software. The ground settlement profile was obtained by selecting a cross-section in the middle of the ground surface DTM (the A-A cross-section in Fig. 8a). Fig. 8 presents a typical example of the ground surface DTM and the selected ground settlement profile. The precision of this technique compared with LVDT readings is within ± 0.3 mm. The same technique was also adopted by Li et al. (2019) to analyze the interaction between group piles and fault movement in a physical test.

After obtaining the ground settlement profile, the angular distortion caused by ground differential settlement was calculated using

$$\beta_{ij} = \frac{\delta_{ij}}{l_{ij}} \tag{1}$$

where δ_{ij} = differential settlement between reference points i and j and l_{ij} = distance between i and j. The maximum angular distortion β_{max} was determined as the maximum value of β along the ground surface, which also represents the steepest slope of the ground settlement profile. Because the angular distortion critically influences the serviceability and damage of superstructures, the β_{max} value was used a key indicator for evaluating the performance of reinforced foundations.

As the fault displaces, the shear rupture propagates upward from the fault tip to the ground surface, causing a distinct shear rupture at the ground surface (Bray, 2001). This rupture is often associated with a significant angular distortion at the ground surface. In this study, the shear rupture propagation within the foundation model was observed from a series of high-resolution images taken during the tests. The successive digital images were analyzed to obtain the displacement and strain fields of soil using Ncorr (Blaber et al., 2015), an open source 2D digital image correlation (DIC) software featured in high strain analysis. The DIC analysis was facilitated by seeding black colored sands in the foundation model as tracer particles. The development of shear strain contour as the fault displacement increased was selected to represent the shear rupture propagation within the foundation model. The influence of reinforcement inclusion on the shear rupture propagation was examined and discussed.

The tensile strain distribution along each reinforcement was determined using the technique proposed by Zornberg and Arriage (2003). First, digital images taken during tests were used to determine the change in the coordinates of plastic markers that were attached to the reinforcement as fault displacement increased. The left boundary of the sandbox provided a reference point that did not move during tests. The accumulative displacement of reinforcement for the increasing fault displacement was then obtained by calculating the increase in displacement of each marker relative to the reference point (Fig. 9a). A sigmoid function was then adopted to fit the accumulative displacement curve of reinforcement (the dashed lines in Fig. 9a)

$$d(x) = \frac{1}{a + be^{-cx}} \tag{2}$$

where d = accumulative displacement of each marker relative to the reference point; x = distance to the left boundary; a, b, and c = fitting constants; and e = natural exponential function. The reason for fitting the displacement curve was to avoid the impact of errors made in determining plastic marker positions on the accuracy of calculating reinforcement tensile strain (Zornberg and Arriage, 2003). Finally, the tensile strain distribution of reinforcement was determined by differentiating the sigmoid fitting function (Eq. (2)) with respect to x. Fig. 9b presents a typical example of reinforcement strain distributions at various fault offsets.

3. Results and discussion

3.1. Unreinforced foundation

Fig. 10 presents a series of images of the unreinforced foundation test (Test U) at fault offset S = 0 (initial condition), 1.5, 3, and 6 cm. Test results revealed that the ground deformation became pronounced as the fault movement increased. The development of shear rupture induced by fault movement can be visually identified from the relative

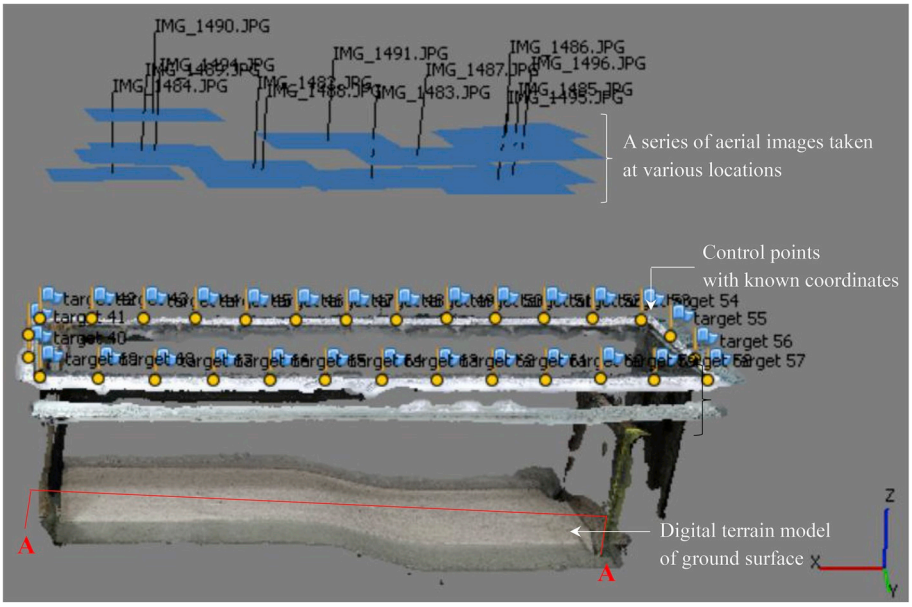

(a)

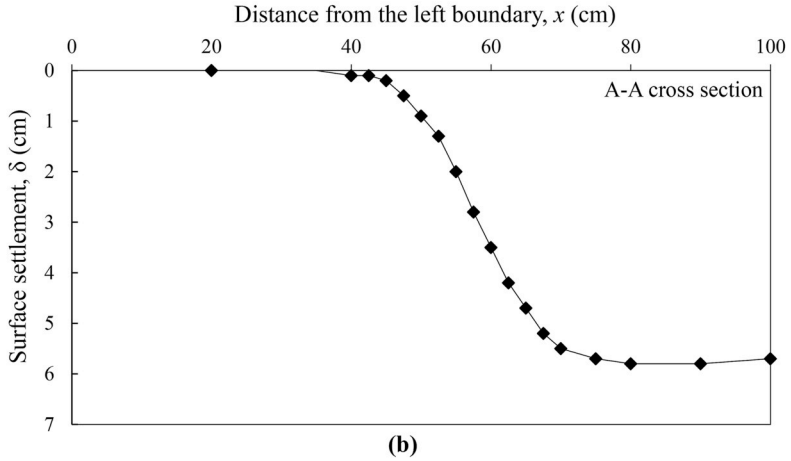

(b)

Fig. 8. Determination of ground surface settlement: (a) digital terrain model; (b) surface settlement profile.

displacement of black colored sand layers added to the foundation model. The first shear rupture SR1 was initiated from the fault tip and propagated upward at $S = 1.5$ cm (Fig. 10a). The SR1 reached the ground surface, and the second/antithetic shear rupture SR2 was initiated at $S = 3$ cm (Fig. 10b). A distinct surface fault rupture occurred at the ground surface at this stage because of the breakthrough of the SR1. The shear band of the SR1 became wider, and the SR2 continuously advanced as fault offset increased to $S = 6$ cm. A clear fault scarp developed, and a gravity graben bordered by the SR1 and SR2 began to form. The fault-induced influence zone was approximately 8.3 cm long (≈1.4 times the fault offset). The slope of the SR1 conforms approximately to the fault dip angle. The slope of the SR2 (≈64°) follows the theoretical value of Rankine's active failure plane (i.e., $45^\circ + \varphi/2$), indicating that active soil failure occurred as the hanging wall moved apart from the footwall. The preceding discussion of fault rupture propagation of the unreinforced foundation agrees with the centrifuge test results (Anastasopoulos et al., 2007, 2009) and field observations (Bray et al., 1994).

Fig. 11a–c shows variations in surface settlement δ, maximum angular distortion β_{max}, and overburden pressure σ_v with fault offset, respectively. The maximum surface settlement δ_{max} occurred at the middle of the fault graben, approximately at a location vertically above the fault tip (Fig. 11a). The δ_{max} values were 2.5, 4, 5.5, and 7.2 cm at $S = 1.5$, 3, 4.5, and 6 cm, respectively. Notably, the δ_{max} value at each fault offset stage was larger than the corresponding fault offset because of the influence from the fault displacement in both vertical and horizontal directions. The maximum angular distortion β_{max} values were 0.40, 0.48, 0.61, and 0.72 at $S = 1.5$, 3, 4.5, and 6 cm, respectively (Fig. 11b). The β_{max} increased as the fault displacement increased and became close to the slope of the angle of repose of the sand ($= \tan\varphi = 0.8$) at large fault offset. The overburden pressure σ_v measured by PC1 shows an increasing trend at $S < 3$ cm and then a decrease to an equilibrium state at $S \geq 3$ cm (Fig. 11c). The increasing trend of σ_v at $S < 3$ cm can be attributed to the influence of the downdrag force from the failed soil mass near the SR1 acting on the PC1, causing the measured σ_v to be higher than the theoretical value ($= \gamma H$). The decrease in σ_v was caused by the increasing surface settlement within the fault influence zone as the SR2 developed and the fault graben formed when $S \geq 3$ cm (see Figs. 10 and 11a). The σ_v measured by PC2 shows a constant trend that complies with the theoretical value. This constant trend indicates that the fault movement has no impact on the overburden pressure of the soil located outside the fault influence zone.

3.2. Reinforced foundation

Fig. 12 presents a series of images of the reinforced foundation test

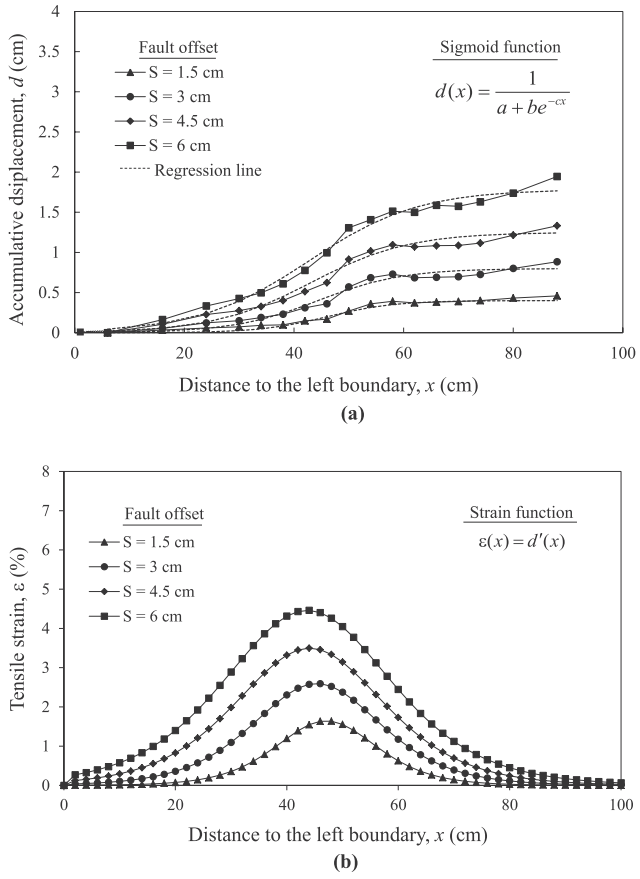

Fig. 9. Determination of mobilized reinforcement tensile strain (Layer 3 of Test R-3L-2J): (a) sigmoid function for fitting displacement curve; (b) strain function for calculating tensile strain.

(Test R-3L), the baseline case, at various fault offsets. A smooth ground settlement profile was observed as the fault displaced. The ground surface gradually settled and reached a δ_{max} value equal to the corresponding fault offset. The fault-induced influence zone of the reinforced foundation (≈21.5 cm) was wider than that of the unreinforced zone

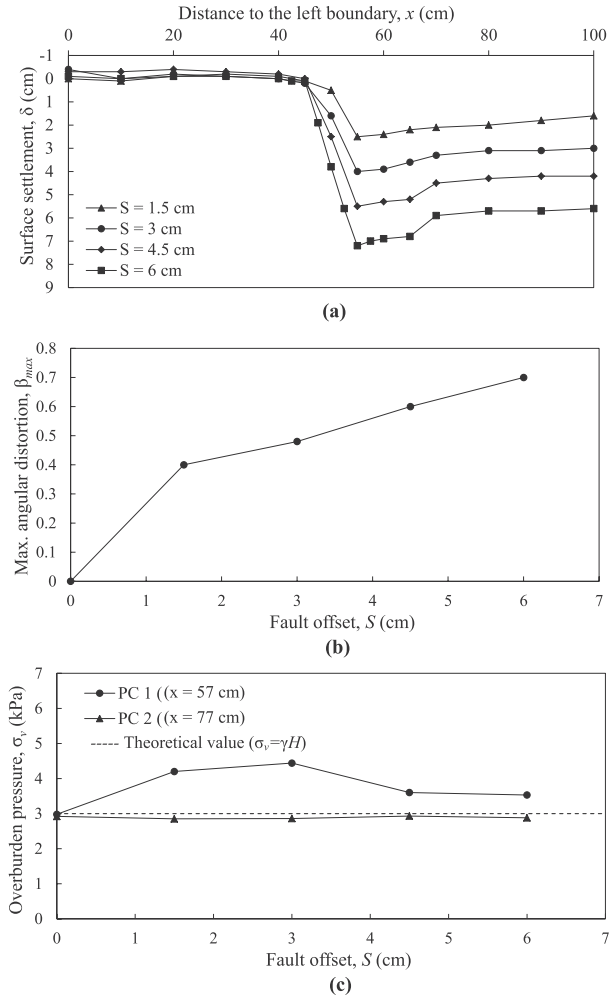

Fig. 11. Results of the unreinforced foundation test at various fault offsets: (a) surface settlement profile; (b) maximum angular distortion; (c) overburden earth pressure.

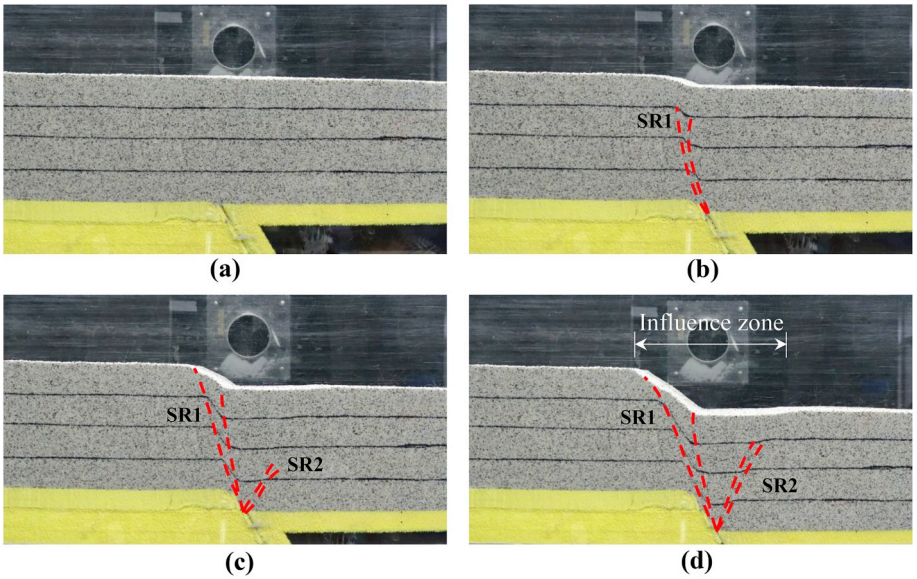

Fig. 10. Photos of the unreinforced foundation test (Test U) at various fault offsets: (a) $S = 0$ cm; (b) $S = 1.5$ cm; (c) $S = 3$ cm; (d) $S = 6$ cm.

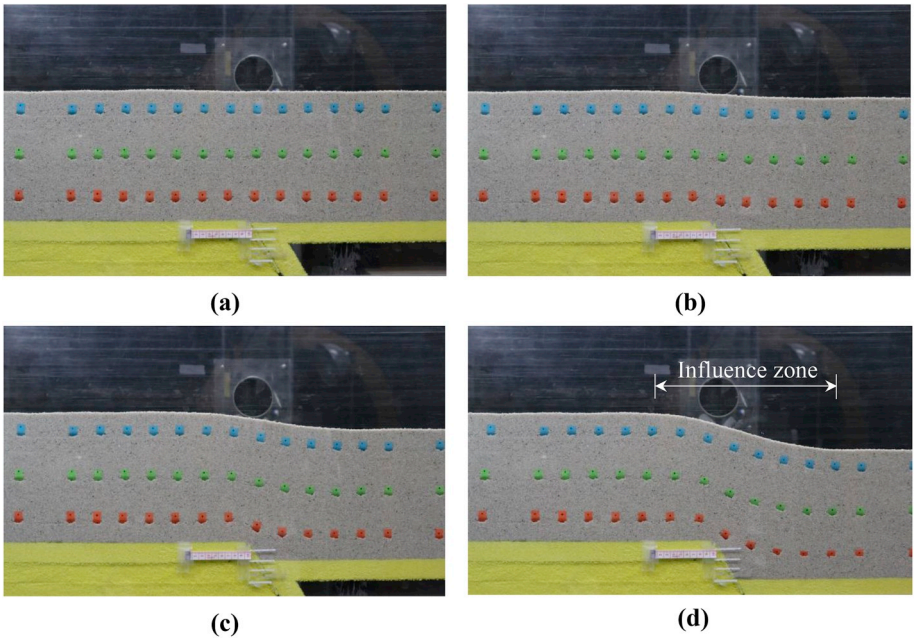

Fig. 12. Photos of the reinforced foundation test (Test R-3L) at various fault offsets: *(a)* $S = 0$ cm; (b) $S = 1.5$ cm; (c) $S = 3$ cm; (d) $S = 6$ cm.

(≈8.3 cm), suggesting that the differential settlement induced by fault movement was spread across a wider zone in the soil. Distinct surface fault rupture did not occur until the end of the test.

Fig. 13a–c shows variations in δ, β_{max}, and σ_v with fault offset, respectively. The β_{max} increased linearly with fault offset. The β_{max} values were 0.08, 0.17, 0.22, and 0.28 at $S = 1.5$, 3, 4.5, and 6 cm, respectively (Fig. 13b). The β_{max} value for the reinforced foundation was significantly lower than (on average 60%) that for the unreinforced foundation at the same fault offset. The test results show that the reinforcement inclusions have a substantial effect on reducing the fault induced angular distortion. A decreasing trend of the σ_v measured by PC1 was observed, which is opposite to the increasing trend in unreinforced foundations (Fig. 13c). The decreasing trend pertains to the tensioned membrane effect of reinforcement that supported the overlying soil and counterbalanced the vertical overburden pressure, resulting in the measured σ_v close to the fault rupture being lower than the theoretical value. The fault movement had a negligible effect on σ_v measured by PC2, which was located far from the fault rupture. The reason for this observation is similar to that for the unreinforced foundation explained previously.

Fig. 14 shows the mobilized tensile strain for each reinforcement layer. The mobilized tensile strain of reinforcement increased as fault movement increased. The peak of the tensile strain distribution along each reinforcement layer was located approximately above the fault tip. The mobilized reinforcement tensile strain increased with depth and reached a maximum value at the bottommost reinforcement layer, which was the closest to the fault and had most direct influence by the fault. Fig. 14c shows that the maximum tensile strains determined by the DIA technique (Zornberg and Arriage, 2003) and residual strain method (Nguyen et al., 2013) are in good agreement. Notably, the residual strain method was developed for nonwoven geotextile under in-isolation conditions, and the DIA technique measured the mobilized tensile strain of nonwoven geotextile under in-soil conditions. This consistency demonstrated that the soil confinement has a minor effect on the mobilized tensile strain level of the nonwoven geotextile. This comparison also mutually verifies the correctness of these methods used to determine the reinforcement tensile strains in this study. Furthermore, careful inspection of retrieved reinforcement layers after the test showed there was no reinforcement breakage. This finding can be justified by the fact that the maximum mobilized tensile strain of

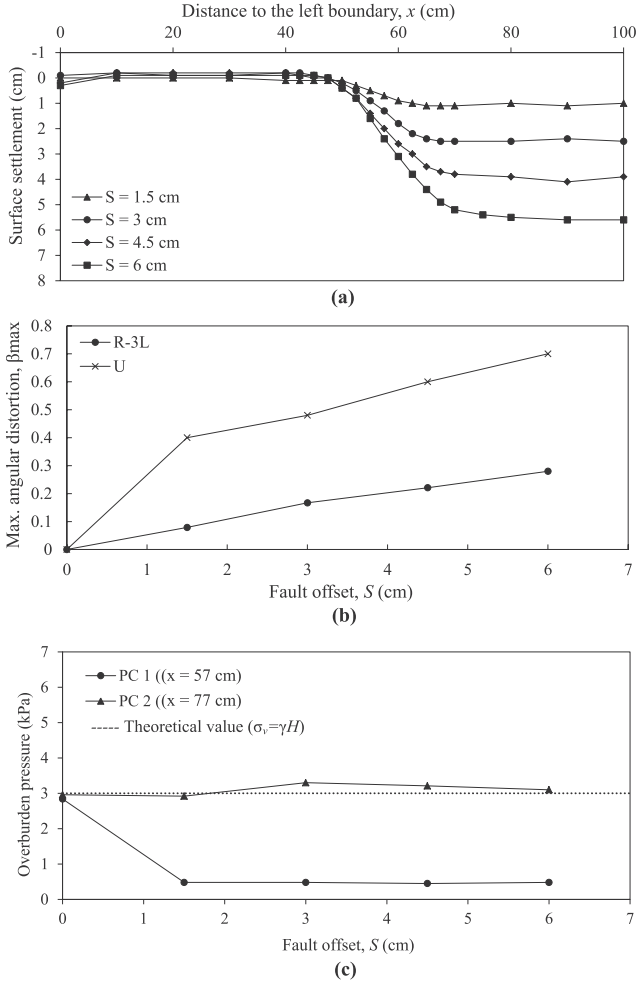

Fig. 13. Results of the reinforced foundation test (Test R-3L) at various fault offsets: (a) surface settlement profile; (b) maximum angular distortion; (c) overburden earth pressure.

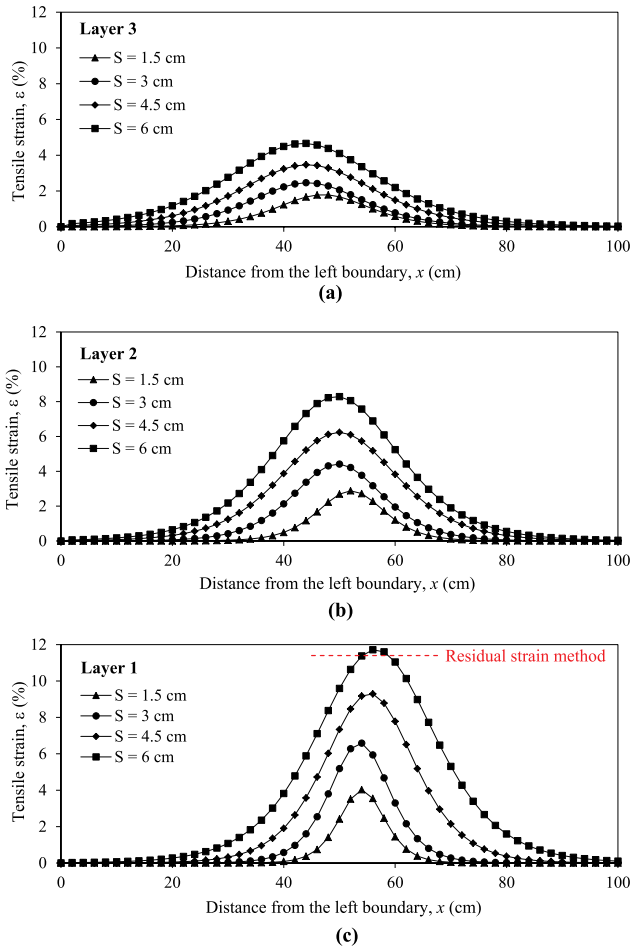

Fig. 14. Mobilized reinforcement tensile strain of the reinforced foundation test (Test R-3L): (a) Layer 3; (b) Layer 2; (c) Layer 1.

reinforcement layer 1 at $S = 6$ cm ($\varepsilon = 11.7\%$) had still not reached the failure strain determined from the wide-width tensile test ($\varepsilon_f = 32.4\%$ in Fig. 6).

Fig. 15 shows the shear strain contours for both unreinforced and reinforced foundations. The shear strain contours were analyzed using the DIC software, Ncorr (Blaber et al., 2015), to discern the development of a shear band within the foundation model. For the unreinforced foundation (Fig. 15a–c), the shear band propagated upward from the fault tip to the ground surface as the fault displaced. The contour of the intense shear strain reached the ground surface at $S = 3$ cm, indicating that the shear rupture had broken through the foundation soil and a surface fault rupture had occurred at the ground surface. The development of shear strain contours also matches the visual observation of SR1 discussed in Section 3.1. For the reinforced foundation (Fig. 15d–f), the shear band also propagated upward as the fault displaced and reached reinforcement layer 3, the topmost layer, at $S = 3$ cm. As fault displacement increased to $S = 6$ cm, the shear band became broader but did not propagate any further (it stopped at reinforcement layer 3). Test results demonstrated that reinforcement inclusions could effectively interrupt the shear rupture propagation and prevent it from reaching the ground surface to cause a surface fault rupture. Notably, intense shear strain contours also developed along three reinforcement layers, indicating that a strong soil-reinforcement interaction took place for the mobilization of the reinforcement tensile forces (Fig. 14).

In summary, this study identified the following three mechanisms provided by reinforcement inclusion that prevented the surface fault rupture and significantly reduced fault-induced angular distortion at the ground surface:

1. support the overlying soil by a tensioned membrane effect through reinforcement tensile force mobilization to produce a gradual and smooth ground settlement profile,
2. interrupt shear rupture propagation reaching the ground surface to prevent the occurrence of a surface fault rupture, and
3. spread the fault-induced differential movement across a wider zone in the fill to reduce the angular distortion at the ground surface.

4. Parametric study

This study evaluated the effect of reinforcement parameters (i.e., the number of reinforcement layers, reinforcement stiffness, and location) and foundation height on the performance of reinforced foundations subjected to fault displacement. Compared with the unreinforced foundation, the effect of each reinforcement or foundation parameter on reducing the β_{max} was quantified by the percentage reduction R_d expressed as follows:

$$R_d = \frac{\beta_{max,\,u} - \beta_{max,\,r}}{\beta_{max,\,u}} \tag{3}$$

where $\beta_{max,\,u}$ = maximum angular distortion of the unreinforced foundation and $\beta_{max,\,r}$ = maximum angular distortion of the reinforced foundation with each investigated parameter. Test results for the parametric study are summarized in Table 1 and discussed in this section.

4.1. Reinforcement location

Fig. 16 shows the test results for the influence of reinforcement location at various fault offsets. Tests R-1L-1/4E, R-1L-1/2E, and R-1L-3/4E indicate the reinforced foundation with one single reinforcement layer located at the bottom quarter, middle, and top quarter of the foundation height, respectively. The test results for Test R-1L-1/4E, the case with the reinforcement layer placed close to the bedrock fault, show that the surface settlement profile was non-smooth (Fig. 16a), and the β_{max} values were significantly larger than those in the other two tests (Fig. 16b). The β_{max} values were 0.42, 0.32, 0.302, and 0.72 and the R_d values were 42%, 56%, and 58% for Tests R-1L-1/4E, R-1L-1/2E, and R-1L-3/4E at $S = 6$ cm, respectively (Table 1). As shown in Fig. 17, the jagged ground surface of Test R-1L-1/4E indicated that the shear ruptures had broken through the foundation soil and a surface fault rupture had occurred at the ground surface. The first distinct surface fault rupture appeared at $S = 3$ cm (Fig. 17c) and the second at $S = 6$ cm (Fig. 17d). By contrast, surface fault ruptures were not observed in Tests R-1L-1/2E and R-1L-3/4E where the reinforcement layer were installed at a distance above the bedrock fault. The subpar performance of Test R-1L-1/4E was attributed to the fact that the deformation pattern of the reinforcement was governed by the displacement boundary at the bedrock fault. When the reinforcement was placed close to the bedrock fault, the reinforcement and fault displaced together in a similar manner; consequently, the reinforcement turned out to be less efficacious in preventing the shear rupture propagation.

Fig. 16c shows the variation in the mobilized maximum reinforcement strain ε_{max} with various fault offsets. At a given S, the ε_{max} value increased as the reinforcement layer was located closer to the fault. This result was due to the impact from the displacement boundary. For the reinforcement layer that was installed at a distance above the bedrock fault, the presence of a thick soil layer between the reinforcement and bedrock fault partially absorbed the fault displacement and hence reduced the reinforcement deformation. Moreover, as indicated in Fig. 16c, the ε_{max} values at $S = 6$ cm were 12.2% and 10.7% for Tests R-1L-1/4E and R-1L-1/2E, respectively, which match the values ($\varepsilon_{max} = 11.8\%$ and 10.7%, respectively) estimated using the residual

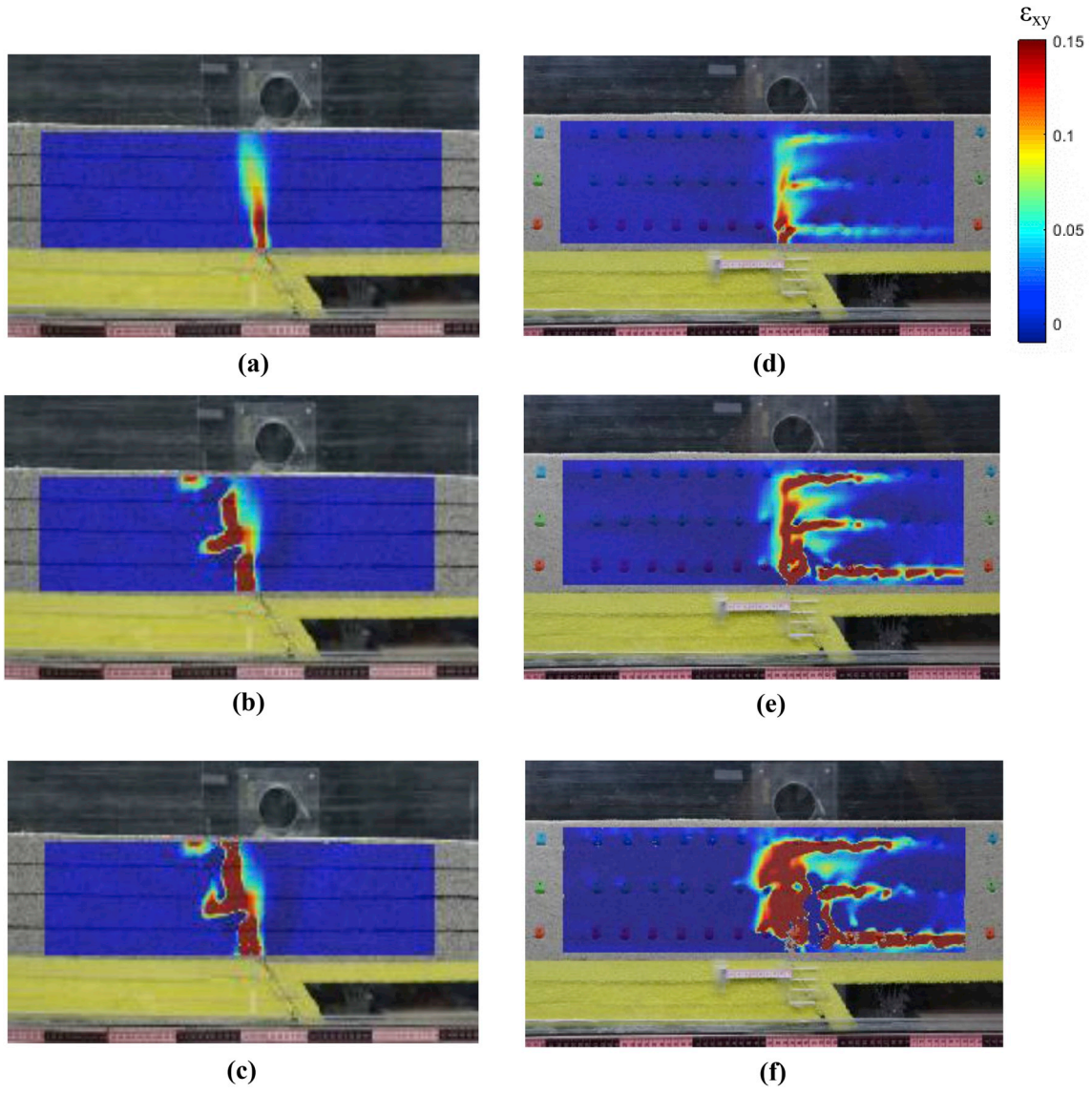

Fig. 15. Shear strain contour of the unreinforced foundation (Test U) at: (a) $S = 0.75$ cm; (b) $S = 1.5$ cm; (c) $S = 3$ cm; and shear strain contour of the reinforcement foundation test (Test R-3L) at: (d) $S = 1.5$ cm; (e) $S = 3$ cm; (f) $S = 6$ cm.

strain method. Given these results, it can be concluded that placing the reinforcement at a distance above the bedrock fault, at least above the midheight of the foundation, is more effective than placing the reinforcement close to the bedrock fault in mitigating the impact from surface faulting, in terms of reducing the β_{max} and minimizing the mobilization of reinforcement ε_{max}.

4.2. Foundation height

Fig. 18 shows the test results for the influence of foundation height at various fault offsets. Tests R-3L-10H, R-3L, and R-3L-30H included 3-layer geosynthetic-reinforced foundations with foundation heights of 10, 20, and 30 cm (1.5, 3, and 6 m in prototype), respectively. The maximum angular distortions for Tests R-3L-10H, R-3L, and R-3L-30H at $S = 6$ cm were $\beta_{max} = 0.325$, 0.280, and 0.264, and their corresponding percentage reductions were $R_d = 51\%$, 61%, and 63%, respectively (Table 1). These test results revealed that the angular distortion decreased in line with the increase in the foundation height because a thick soil layer was able to absorb more fault displacement (Fig. 18b). The test results in this study agree with the numerical results from finite element analyses conducted by Bray (2001) and Bray et al. (1993). They found that the fill height is a controlling factor in reducing the angular distortion at the ground surface: as the fill height increases, hazards associated with earthquake fault rupture are minimized. The test results in this study also indicated that, at a given *S*, the ε_{max} value increased as the foundation height increased (Fig. 18c). As discussed in Section 3.2 and shown in Fig. 14, the ε_{max} value always occurred at the bottommost reinforcement layer (i.e., Layer 1) for all the reinforced foundation cases. The high ε_{max} value mobilized in the thick foundation likely results from a strong soil-reinforcement interaction caused by a high overburden pressure acting on the bottommost reinforcement layer in the thick foundation.

4.3. Reinforcement stiffness

Fig. 19 shows the test results for the influence of reinforcement stiffness at various fault offsets. Tests R-3L, R-3L-2J, and R-3L-3J included 3-layer geosynthetic-reinforced foundations with the reinforcement stiffness equal to, twice, and triple that in the baseline case, respectively. Doubling or tripling the reinforcement stiffness was achieved by attaching two or three sheets of nonwoven geotextiles together into one layer. Test results showed that the surface settlement

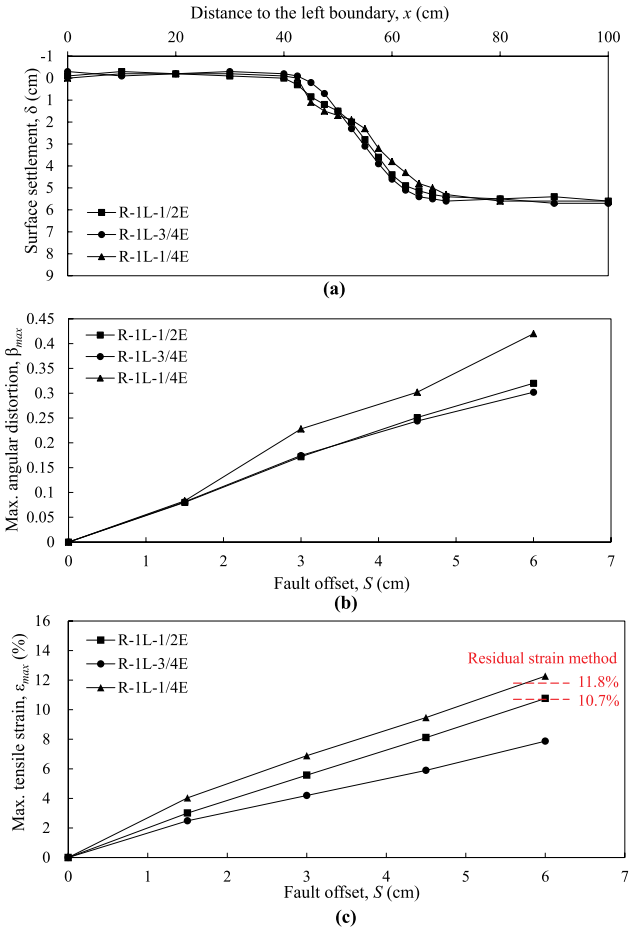

Fig. 16. Results of the influence of reinforcement location: (a) surface settlement profile at S = 6 cm; (b) maximum angular distortion; (c) maximum reinforcement tensile strain.

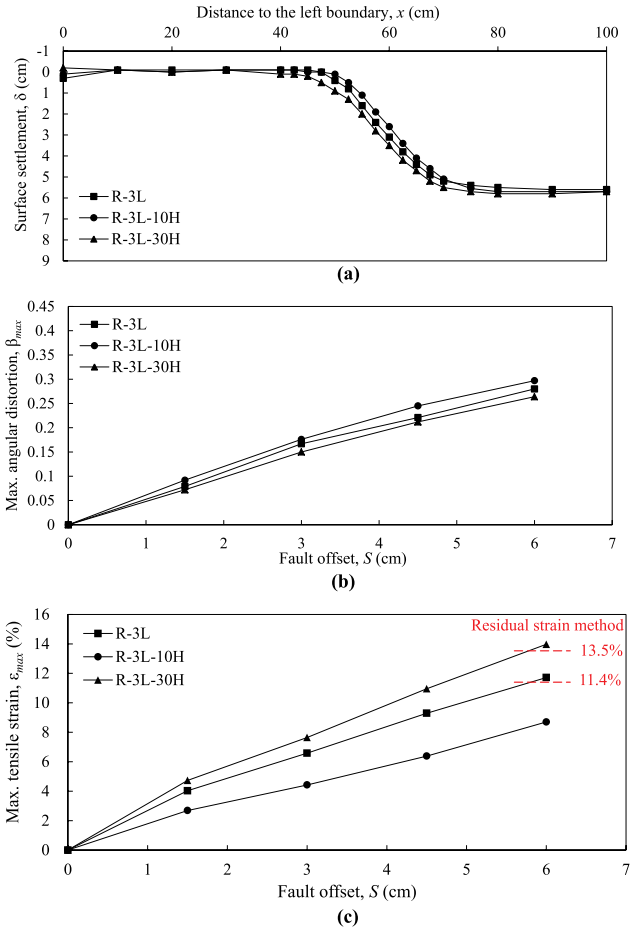

Fig. 18. Results of the influence of foundation height: (a) surface settlement profile at S = 6 cm; (b) maximum angular distortion; (c) maximum reinforcement tensile strain.

profiles of three foundations with different reinforcement stiffness coincided (Fig. 19a). The β_{max} value slightly decreased as the reinforcement stiffness increased (Fig. 19b). The β_{max} values were 0.280, 0.262, and 0.252 and their R_d values were 61%, 64%, and 65% for Tests R-3L, R-3L-2J, and R-3L-3J at S = 6 cm, respectively (Table 1). A comparison of Tests R-3L and R-3L-3J shows that the β_{max} value was reduced by

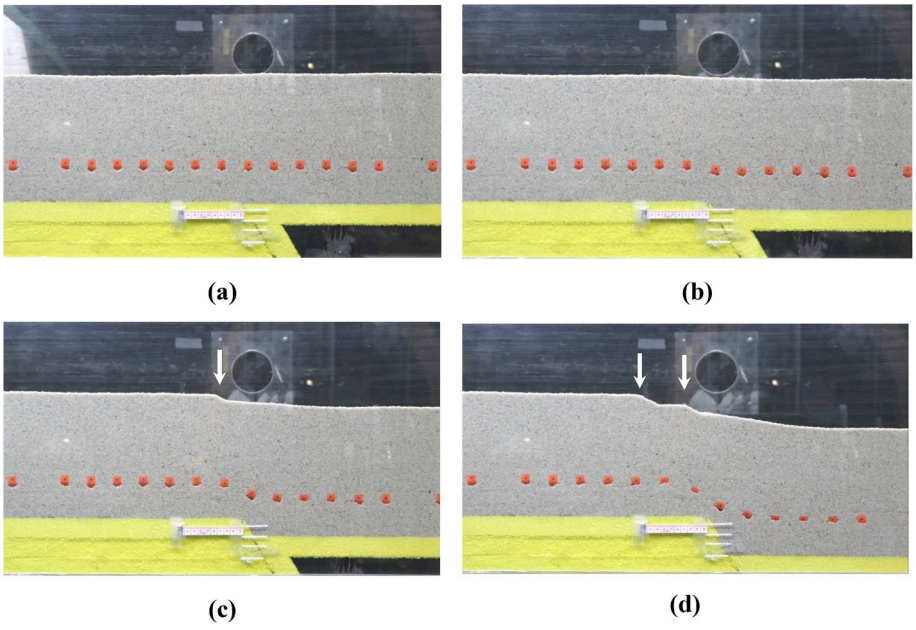

Fig. 17. Development of distinct surface fault ruptures of Test R-1L-1/4E at: *(a)* S = 0 cm; (b) S = 1.5 cm; (c) S = 3 cm; (d) S = 6 cm.

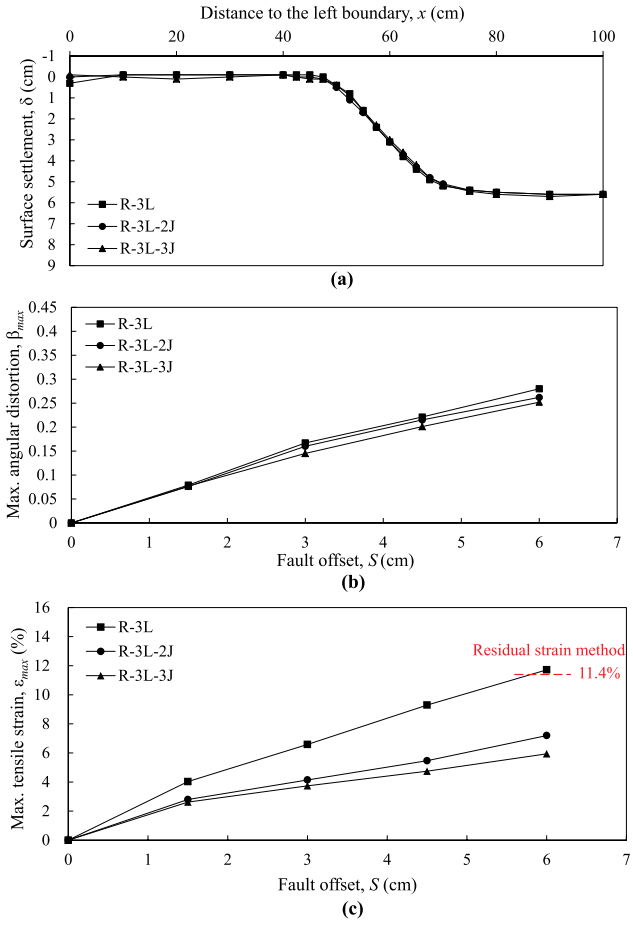

Fig. 19. Results of the influence of reinforcement stiffness: (a) surface settlement profile at S = 6 cm; (b) maximum angular distortion; (c) maximum reinforcement tensile strain.

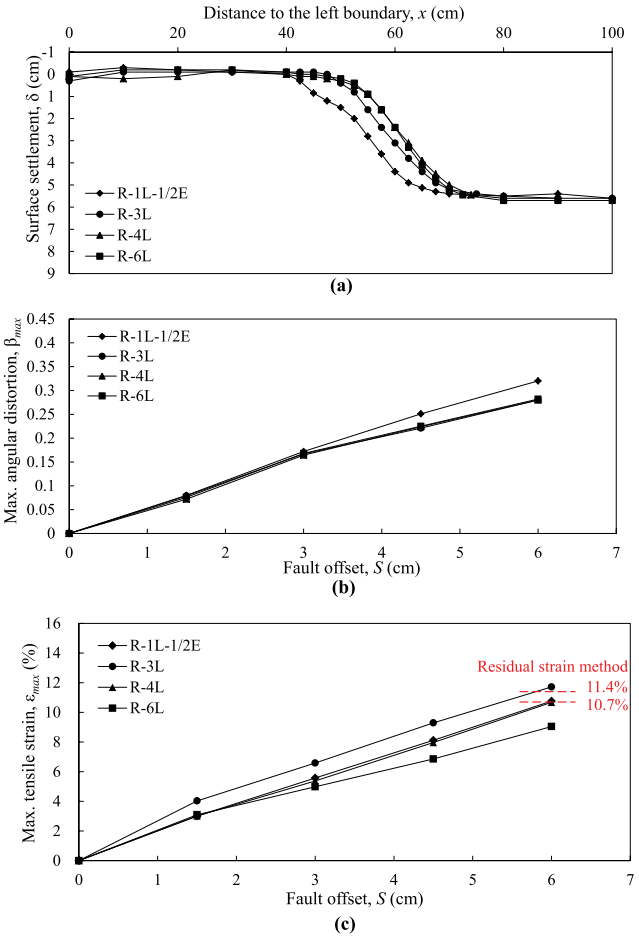

Fig. 20. Results of the influence of number of reinforcement layers: (a) surface settlement profile at S = 6 cm; (b) maximum angular distortion; (c) maximum reinforcement tensile strain.

approximately 10% when the reinforcement stiffness was increased threefold. Test results also showed that the ε_{max} value significantly decreased as the reinforcement stiffness increased (Fig. 19c). For example, at S = 6 cm, the ε_{max} = 11.6% in Tests R-3L decreased to ε_{max} = 5.9% in Test R-3L-3J (Table 1). This result is likely because the stiffer reinforcement deformed less with the same fault movement, resulting in a lower reinforcement tensile strain developing in the reinforced foundation with stiffer reinforcement. Nevertheless, approximately similar magnitudes of reinforcement tensile loads were mobilized in these three reinforced foundation cases, regardless of the stiffness of the reinforcement, producing almost the same ground settlement profile each time.

4.4. Number of reinforcement layers

Fig. 20 shows the test results for the influence of number of reinforcement layers at various fault offsets. Tests R-1L-1/2E, R-3L, R-4L, and R-6L included reinforced foundations with 1, 3, 4, and 6 layers of reinforcement, respectively. Reinforcements in these tests were arranged to ensure equal spacing. As shown in Fig. 20b, the 1-layer geosynthetic-reinforced foundation had the largest β_{max} value. Notably, the number of reinforcement layers had negligible influence on β_{max} as the reinforcement increased from 3 to 6 layers. The β_{max} values were 0.320, 0.280, 0.280, and 0.280 and their R_d values were 56%, 61%, 61%, and 61% for Tests R-1L-1/2E, R-3L, R-4L, R-6L at S = 6 cm, respectively (Table 1). Test results suggested that the 3-layer reinforced foundation had an optimal effect in minimizing the fault-induced angular distortion at ground surface for the test conditions specified in this study. Further increases in reinforcement layers did not lead to any consequential improvement in reducing the angular distortion.

Fig. 20c shows the variation of ε_{max} with various fault offsets. For Tests R-3L, R-4L, and R-6L, the ε_{max} value decreased as the number of reinforcement layers increased. The reason for this result is similar to that discussed previously for the influence of reinforcement stiffness. Compared with those with a smaller number of reinforcement layers, the reinforced foundation with a larger number of reinforcement layers had higher system stiffness and thus could generate less internal deformation with the fault movement. Consequently, the mobilization of reinforcement tensile strain was low in this foundation. It was notable that, at a certain S, the ε_{max} value of the 1-layer geosynthetic-reinforced foundation was lower than that of the 3-layer foundation and only slightly higher than that of the 4-layer foundation. This result can be attributed to the influence of reinforcement location. As discussed in Section 4.1, the ε_{max} value decreased as the distance between the reinforcement and bedrock fault increased. Because the reinforcement of Test R-1L-1/2E was placed at the middle of the foundation, a distance above the bedrock fault, the displacement boundary had less influence on reinforcement strain mobilization.

5. Design implications

This section discusses design suggestions and implications by evaluating the overall performance of reinforced foundations. Fig. 21 shows the relationship between the maximum angular distortion and maximum mobilized reinforcement tensile strain with fault displacement. The fault offset in Fig. 21 is presented in prototype scale up to 0.9 m.

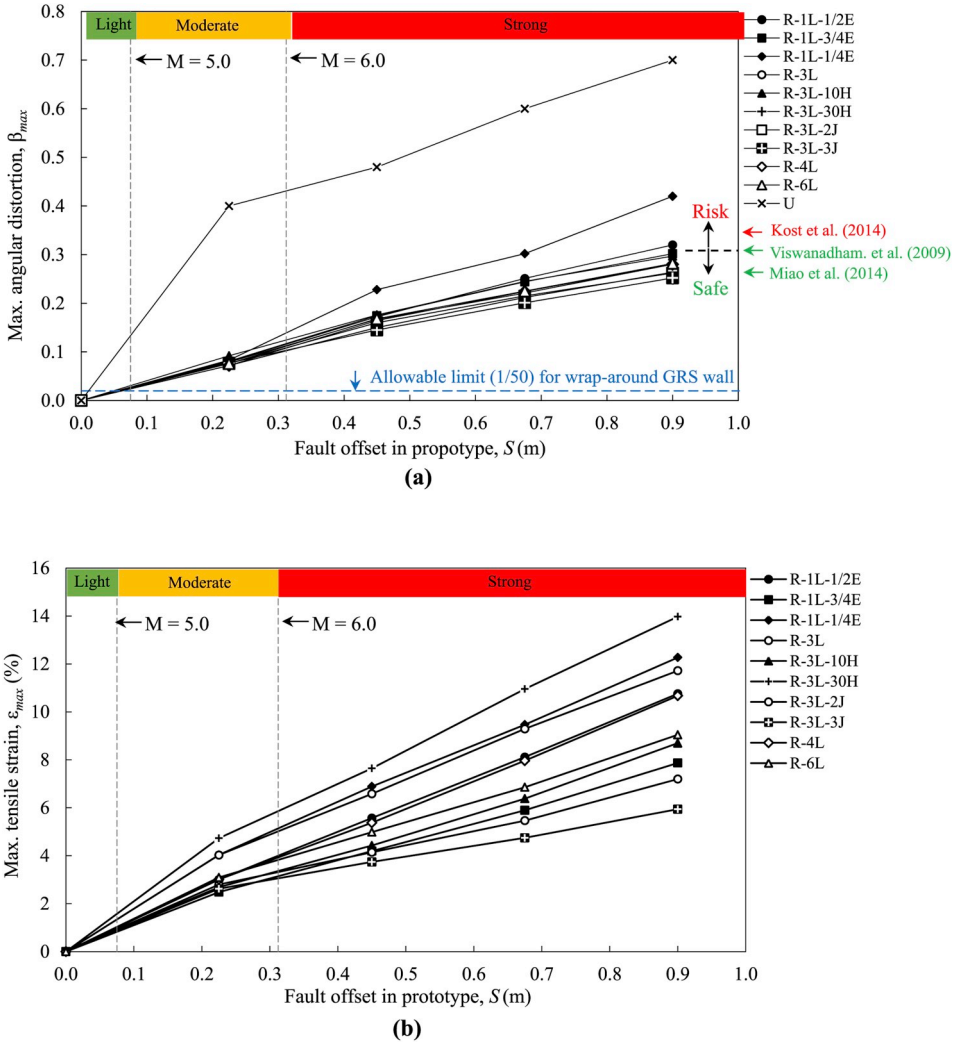

Fig. 21. Overall evaluation of the performance of reinforced foundations: (a) maximum angular distortion; (b) maximum reinforcement tensile strain.

The fault offset is further associated with earthquake magnitude by using the empirical formula published in the U. S. Geological Survey (Bonilla, 1967) based on statistical data for 35 cases of historic faulting of the ground surface in the United States and Mexico. The relationship between the maximum fault displacement and the magnitude of the associated earthquake is expressed as

$$\text{Log } D = 0.57\ M_L – 3.91 \quad (4)$$

where D = maximum displacement in feet and M_L = Richter magnitude. Using Eq. (4), Fig. 21 can be divided into three intervals: light ($M_L < 5.0$), moderate ($5.0 \le M_L < 6.0$), and strong earthquake ($M_L \ge 6.0$), and the associated fault offset $S < 7$ cm, 7 cm $\le S <$ 32 cm, and $S \ge 32$ cm), respectively.

Fig. 21a shows the development of the maximum angular distortion with fault offset for all the tests. For reference, the tolerable/allowable angular distortion for wrapped-around GRS walls was also plotted in Fig. 21a. The allowable angular distortion values for GRS walls were adopted from the design guidelines (Elias et al., 2001; Wu et al., 2006; Holtz et al., 1998) which have suggested that the tolerable angular distortion (or allowable design limit) at the foundation level of the GRS wall is 1/200 for modular block walls and 1/50 for wrapped face walls. The angular distortion limits for no evident damage of GRS structures were also indicated in Fig. 21a. The values of the angular distortion limits were selected from the test results reported in the past studies on GRS walls subjected to differential settlement (Viswanadham and Konig, 2009; Kost et al., 2014; Miao et al., 2014). Table 4 summarizes the test conditions and results for these studies. These test results show that, for wrapped-around GRS walls, the integrity and stability of the wall system remained and no evident damage was observed at the end of tests as the β_{max} was applied up to 0.260 in Miao et al. (2014) and 0.313 in Viswanadham and Konig (2009). For GRS walls with modular block facing, local failure of the wall occurred (severely distressed, and several diagonal cracks developed) as the β_{max} reached 0.345 (Kost et al., 2014).

Test results in Fig. 21a suggest that for a fault movement in a prototype less than 7 cm (corresponding to light earthquake with $M_L < 5$), the measured β_{max} values of all reinforced foundations were approximately within the allowable limit for wrapped-around GRS walls (1/50). For fault movements ranging from 7 to 90 cm (corresponding to moderate and strong earthquake with M_L = 5–7), although the measured β_{max} values exceeded the allowable limit, the β_{max} values of the reinforced foundations with more than one reinforcement layer were still below the range of no evident damage observed for wrapped-around GRS structures in the past studies (Miao et al., 2014; Viswanadham and Konig, 2009). This result indicates that a wrapped-around GRS structure seated on a reinforced foundation can still maintain its stability and serviceability when a moderate or strong earthquake occurs. Based on the discussion on Fig. 21a, when it is necessary to construct a highway embankment across a fault, an integrated system consisting of a wrapped-around GRS embankment

Table 4
Summary of test conditions and results of GRS structures subjected to differential settlement from the past studies.

Case	Kost et al. (2014)	Miao et al. (2014)	Viswanadham and Konig (2009)
Structural type	Abutment	Embankment	Slope
Model scale (model/prototype)	Full-scale (1/1)	Reduced scale (1/12)	Centrifuge (1/40)
[a]Height (m)	3.1	2.4	10.8
Facing type	Modular block	Wrapped-around	Wrapped-around
Facing inclination (°)	90	64	34
[a]Differential settlement (m)	0.4	0.32	1
Maximum angular distortion	0.345	0.260	0.313
Test results	Local failure	No evident damage	No evident damage

[a] dimension in prototype.

overlying a reinforced foundation is recommended to mitigate hazards associated with earthquake fault rupture.

Fig. 21b shows the mobilization of the maximum reinforcement tensile strain with fault offset for all the tests, which provides important design information regarding the selection of reinforcement properties against breakage. When designing a reinforced foundation subjected to surface faulting, the following criterion should be satisfied to prevent reinforcement breakage:

$$\varepsilon_{ult} > \varepsilon_{max} \quad (5)$$

where ε_{ult} = reinforcement ultimate tensile strain at failure and ε_{max} = mobilized maximum reinforcement tensile strain corresponding to a certain magnitude of fault displacement. If this criterion is violated, the reinforcement could rupture and hence become invalid in preventing the shear rupture propagation that causes a surface fault rupture. As shown in Fig. 21b, the ε_{max} value increased with S but was significantly influenced by reinforcement parameters and foundation height. At S = 90 cm in the prototype, the reinforcement in Test R-3L-3J had the lowest ε_{max} value (= 5.9%), whereas the reinforcement in Test R-3L-30H had the highest ε_{max} value (= 14.0%) for the test conditions specified in this study. Because ε_{max} appears to vary widely with test conditions, no unique regression equation could be developed to characterize the relationship between ε_{max} and S. Future research is need to assess the influence of a wider range of reinforcement parameters and foundation geometry on ε_{max} and to develop design methods to estimate the mobilization of ε_{max} under various reinforcement and foundation conditions.

6. Conclusions

A series of model tests on GRS foundations across a normal fault were performed to evaluate the performance of the reinforced foundations as a mitigation measure for surface faulting hazards. Digital image analysis techniques were applied to determine the ground settlement profile, angular distortion, shear rupture propagation, and mobilized reinforcement tensile strain at various magnitudes of fault offset. The effects of reinforcement parameters and foundation height on reducing the maximum angular distortion at the ground surface were evaluated quantitatively. Based on the experimental results, the key findings are as follows:

- For unreinforced foundations, the shear ruptures induced by fault movement developed from the fault tip and propagated upward. A distinct surface fault rupture occurred at the ground surface because of the breakthrough of the shear rupture. As the fault offset reached 15% of the foundation height, a secondary shear rupture developed in the hanging wall and generated a graben at the ground surface. The fault-induced influence zone was approximately 1.4 times the failure offset. The maximum angular distortion β_{max} increased as the fault displacement increased and became close to the slope of the angle of repose of the sand at large fault offset.
- For the baseline reinforced foundation case, a smooth ground settlement profile was observed as the fault displaced. The reinforcement inclusions effectively prevented the shear rupture propagating to the ground surface and also spread the differential settlement to a wider influential zone, resulting in an average reduction of 60% in the fault-induced angular distortion at the ground surface as compared with the unreinforced foundation. The measured vertical earth pressure close to the fault rupture was lower than the theoretical value because of the tensioned membrane effect provided by reinforcement to support the overburden pressure of the overlying soil.
- For all reinforced foundation cases, the mobilized tensile strain of reinforcement increased as fault movement increased. The mobilized reinforcement tensile strain increased with depth and reached a maximum value at the bottommost reinforcement layer, which was the closest to the fault. For the baseline case, a maximum tensile strain of 11.6% was observed at the bottommost reinforcement layer when the fault offset reached 6 cm in the model test, equivalent to 90 cm in the prototype
- The results of the parametric study show that the β_{max} decreased as the foundation height, number of reinforcement layer, and reinforcement stiffness increased.
- The results of the parametric study suggest that a reinforced foundation with three reinforcement layers has an optimal effect in minimizing the fault-induced angular distortion at ground surface. Further increases in reinforcement layers did not lead to any consequential improvement in reducing the angular distortion.
- Based on the relation between the maximum fault displacement and the magnitude of the associated earthquake, the β_{max} of the reinforced foundation is still within the allowable limit (1/50) for wrapped-around GRS wall under a light earthquake (M_L < 5) and below the range of no evident damage observed for wrapped-around GRS structures under moderate and strong earthquakes (M_L = 5–7).
- The maximum mobilized reinforcement tensile strain ε_{max} was significantly influenced by reinforcement parameters and foundation height. Because the ε_{max} appears to vary widely with test conditions, no unique regression equation could be developed to characterize the relationship between ε_{max} and fault offset in this study.

Notably, the earthquake-induced structural damage could be caused by both fault movement and ground acceleration. This study only focuses on the effect of fault movement on ground deformation (i.e, surface rupture, and angular distortion). The effect of earthquake-induced ground acceleration on structural stability is not evaluated in this study as it is beyond the scope of this study. In addition, the test results of this study were only applied to the field condition whereby the reinforcement was long enough to avoid the occurrence of reinforcement pullout. The influence of reinforcement length on the performance of reinforced foundations is a noteworthy topic for future research.

Acknowledgement

The research idea was inspired by a real project of a GRS structure

across an active fault designed by Sinotech Engineering Consultants. The authors sincerely appreciate Mr. Zhong-Ru Ruan, the senior engineer in this company, for providing the design information and discussing the design details. This research was supported by Ministry of Science and Technology, Taiwan under the grant number MOST107-2628-E-002-003-MY3.

Notation

a, b, c	fitting constants for sigmoid function (dimensionless)
c'	effective cohesion (kPa)
d	accumulative displacement of each marker relative to the reference point (m)
D	maximum fault displacement (m)
D_r	relative density (%)
D_{50}	mean particle size (m)
e	natural exponential function (dimensionless)
E_φ	efficiency factor (dimensionless)
G_s	specific gravity (dimensionless)
H	foundation height (m)
$J_{50\%}$	reinforcement stiffness (kN/m)
l_{ij}	distance between reference points i and j (m)
L	number of reinforcement layers (dimensionless)
M_L	Richter magnitude (dimensionless)
N	scaling factor (dimensionless)
R_d	percentage reduction of maximum angular distortion (%)
S	fault offset (m)
T	reinforcement tensile force (kN/m)
T_{ult}	reinforcement ultimate tensile strength (kN/m)
x	distance to the left boundary (m)
β_{ij}	angular distortion between reference points i and j (dimensionless)
β_{max}	maximum angular distortion (dimensionless)
$\beta_{max,\ r}$	maximum angular distortion of reinforced foundation (dimensionless)
$\beta_{max,\ u}$	maximum angular distortion of unreinforced foundation (dimensionless)
γ	unit weight of the soil (kN/m^3)
γ_d	dry unit weight (kN/m^3)
$\gamma_{d,\ max}$	maximum dry unit weight (kN/m^3)
$\gamma_{d,\ min}$	minimum dry unit weight (kN/m^3)
δ'	effective interface friction angle (degree)
δ_{ij}	differential settlement between reference points i and j (m)
δ_{max}	maximum surface settlement (m)
ε	reinforcement tensile strain (%)
ε_a	axial strain (%)
ε_f	reinforcement tensile strain at failure (%)
ε_r	residual reinforcement tensile strain (%)
ε_v	volumetric strain (%)
ε_{ult}	reinforcement ultimate tensile strain (%)
ε_{max}	mobilized maximum reinforcement tensile strain (%)
σ_3	confining pressure (kPa)
σ_d	deviatoric stress (kPa)
σ_v	overburden pressure (kPa)
φ'	effective peak friction angle (degree)

References

Anastasopoulos, I., Gazetas, G., Bransby, M.F., Davies, M.C.R., El Nahas, A., 2007. Fault rupture propagation through sand: finite element analysis and validation through centrifuge experiments. J. Geotech. Geoenviron. Eng. ASCE 133 (8), 943–958.

Anastasopoulos, I., Gazetas, G., Bransby, M.F., Davies, M.C.R., El Nahas, A., 2009. Normal fault rupture interaction with strip foundations. J. Geotech. Geoenviron. Eng. ASCE 135 (3), 359–370.

Ardah, A., Abu-Farsakh, M.Y., Voyiadjis, G.Z., 2018. Numerical evaluation of the effect of differential settlement on the performance of GRS-IBS. Geosynth. Int. 25 (4), 427–441.

Argyrou, C., O'Rourke, T.D., Stewart, H.E., Wham, B.P., 2019. Large-scale fault rupture tests on pipelines reinforced with cured-in-place linings. J. Geotech. Geoenviron. Eng. ASCE 145 (3) 04019004.

Ashtiani, M., Ghalandarzadeh, A., Mahdavi, M., Hedayati, M., 2018. Centrifuge modeling of geotechnical mitigation measures for shallow foundations subjected to reverse faulting. Can. Geotech. J. 55 (8), 1130–1143.

ASTM D4595. Standard Test Method for Tensile Properties of Geotextiles by the Wide-Width Strip Method. *ASTM Standards*, ASTM International, West Conshohocken, Pennsylvania, USA.

Ballegeer, J.P., Wu, J.T.H., 1993. In: Cheng, S.C.J. (Ed.), Intrinsic Confined and Unconfined Load-Deformation Properties of Geotextiles. *Geosynthetic Soil Reinforcement Testing Procedures*, ASTM STP 1190. American Society for Testing and Materials, Philadelphia, PA, pp. 16–31.

Bergado, D.T., Shivashankar, R., Sampaco, C.L., Alfaro, M.C., Anderson, L.R., 1991. Behavior of a welded wire wall with poor quality, cohesive-friction backfills on soft Bangkok clay: a case study. Can. Geotech. J. 28 (6), 860–880.

Blaber, J., Adair, B., Antoniou, A., 2015. Ncorr: open-source 2D digital image correlation Matlab software. Exp. Mech. 55 (6), 1105–1122.

Bonilla, M.G., 1967. Historic Surface Faulting in the Continental United States and Adjacent Parts of Mexico. U.S. Geological Survey TID-24124.

Bray, J.D., Ashmawy, A., Mukhopadhyay, G., Gath, E.M., 1993. Use of geosynthetics to mitigate earthquake fault rupture propagation through compacted fill. In: Proceedings of the Geosynthetics '93 *Conference*, (Vancouver, Canada).

Bray, J.D., Seed, R.B., Cluff, L.S., Seed, H.B., 1994. Earthquake fault rupture propagation through soil. J. Geotech. Eng., ASCE 120 (3), 543–561.

Bray, J.D., 2001. Developing mitigation measures for the hazards associated with earthquake surface fault rupture. In: A Workshop on Seismic Fault-Induced Failures-Possible Remedies for Damage to Urban Facilities. Japan Society for Promotion of Science, University of Tokyo, Japan.

Chen, J.F., Tolooiyan, A., Xue, J.F., Shi, Z.M., 2016. Performance of a geogrid reinforced soil wall on PVD drained multilayer soft soils. Geotext. Geomembranes 44 (3), 219–229.

Chen, Y.G., Chen, W.S., Lee, J.C., Lee, Y.H., Lee, C.T., 2001. Surface rupture of 1999 Chi-Chi earthquake yields insights on active tectonics of central Taiwan. Bull. Seismol. Soc. Am. 91 (5), 977–985.

Divya, P.V., Viswanadham, B.V.S., Gourc, J.P., 2017. Centrifuge modeling and digital image cross-correlation analysis of geofiber-reinforced clay-based landfill covers. J. Geotech. Geoenviron. Eng. ASCE 143 (1) 04016076.

Elias, V., Christopher, B.R., Berg, R., 2001. Mechanically Stabilized Earth Walls and Reinforced Soil Slopes Design and Construction Guidelines. National Highway Institute, Federal Highway Administration, Washington, D.C.

Fadaee, M., Ezzatyazdi, P., Anastasopoulos, I., Gazetas, G., 2016. Mitigation of reverse faulting deformation using a soil bentonite wall: dimensional analysis, parametric study, design implications. Soil Dyn. Earthq. Eng. 89, 248–261.

Garcia, F.E., Bray, J.D., 2019a. Discrete element analysis of earthquake fault rupture-soil-foundation interaction. J. Geotech. Geoenviron. Eng. ASCE 145 (9) 04019046.

Garcia, F.E., Bray, J.D., 2019b. Discrete-element analysis of influence of granular soil density on earthquake surface fault rupture interaction with rigid foundations. J. Geotech. Geoenviron. Eng. ASCE 145 (11) 04019093.

Giroud, J.P., Bonaparte, R., Beech, J., Gross, B., 1990. Design of soil layer-geosynthetic systems overlying voids. Geotext. Geomembranes 9 (1), 11–50.

Han, J., Oztoprak, S., Parsons, R.L., Huang, J., 2007. Numerical analysis of foundation columns to support widening of embankments. Comput. Geotech. 34 (6), 435–448.

Helwany, S., Wu, J.T.H., Froessl, B., 2003. GRS bridge abutments - an effective means to alleviate bridge approach settlement. Geotext. Geomembranes 21 (3), 177–196.

Holtz, R.D., Cristopher, B.R., Berg, R.R., 1998. Geosynthetic Design and Construction Guidelines. FHWA HI-95-038. National Highway Institute Federal Highway Administration (FHWA), McLean, Virginia.

Huang, C.C., 2017. Failure mechanisms of steep-faced geosynthetic-reinforced retaining walls subjected to toe scouring. Mar. Georesour. Geotechnol. 35 (8), 1099–1110.

Jiang, K., Gao, F.L., Fang, W., 2012. Treatment mechanism research on the roadbed widening with geosynthetics. Appl. Mech. Mater. 204–208, 1789–1793.

King, L., Bouazza, A., Gaudin, C., O'Loughlin, C.D., Bui, H.H., 2019. Behavior of geosynthetic-reinforced piled embankments with defective piles. J. Geotech. Geoenviron. Eng. ASCE 145 (11) 04019090.

Kost, A.D., Filz, G.M., Cousins, T., Brown, M.C., 2014. Full-scale investigation of differential settlements beneath a GRS bridge. In: Proceedings of Geo-Congress 2014, (Atlanta, USA).

Kuwano, J., Tachibana, S., Ishigaki, T., Tatta, N., 2013. Confined-reinforced subgrade to reduce differential settlement of road pavement. In: Proceedings of 5th KGS-JGS Geotechnical Engineering Workshop, pp. 149–154 (Seoul, Korea).

Lazarte, C.A., Bray, J.D., Johnson, A.M., Lemmer, R.E., 1994. Surface breakage of the 1992 landers earthquake and its effects on structures. Bull. Seismol. Soc. 84 (3), 547–561.

Leshchinsky, D., Field, D.A., 1987. Soil Load Elongation, Tensile Strength and Interface Friction Angle of Nonwoven Geotextiles, vol. 87. Geosynthetics, New Orleans, LA, USA, pp. 238–249.

Li, C.H., Lin, M.L., Huang, W.C., 2019. Interaction between pile groups and thrust faults in a physical sandbox and numerical analysis. Eng. Geol. 252, 65–77.

Ling, H.I., Wu, J.T.H., Tatsuoka, F., 1992. Short-term strength and deformation characteristics of geotextiles under typical operational conditions. Geotext. Geomembranes 11 (2), 185–219.

Loli, M., Kourkoulis, R., Gazetas, G., 2018. Physical and numerical modeling of hybrid foundations to mitigate seismic fault rupture effects. J. Geotech. Geoenviron. Eng. ASCE 144 (11) 04018083.

Marx, D.H., Jacobz, S.W., 2018. Optimal placement of reinforcement in piggyback landfill liners. Geotext. Geomembranes 46 (3), 327–337.

Miao, L., Wang, F., Han, J., Lv, W., 2014. Benefits of geosynthetic reinforcement in widening of embankments subjected to foundation differential settlement. Geosynth. Int. 21 (5), 321–332.
Moosavi, S.M., Jafari, M.K., 2012. Investigation of the Surface Fault Rupture Hazard Mitigation by Geosynthetics. In: Proceedings of the 15th World Conference on Earthquake Engineering, Lisbon, Portugal.
Muir Wood, D., 2004. Geotechnical Modeling. Taylor and Francis.
Nguyen, M.D., Yang, K.H., Lee, S.H., Wu, C.S., Tsai, M.H., 2013. Behavior of nonwoven geotextile-reinforced soil and mobilization of reinforcement strain under triaxial compression. Geosynth. Int. 20 (3), 207–225.
Oettle, N.K., Bray, J.D., 2013. Geotechnical mitigation strategies for earthquake surface fault rupture. J. Geotech. Geoenviron. Eng. ASCE 139 (11), 1864–1873.
Ohta, H., Ishigaki, T., Tatta, N., 2013. Retrofit technique for asphalt concrete pavements after seismic damage. In: *Proceedings Of 18th International Conference On Soil Mechanics And Geotechnical Engineering*, pp. 1333–1336 Paris.
Puppala, A.J., Ruttanaporamakul, P., Congress, S.S.C., 2019. Design and construction of lightweight EPS geofoam embedded geomaterial embankment system for control of settlements. Geotext. Geomembranes 47 (3), 295–305.
Rajesh, S., Viswanadham, B.V.S., 2012. Centrifuge modeling and instrumentation of geogrid-reinforced soil barriers of landfill covers. J. Geotech. Geoenviron. Eng. ASCE 138 (1), 26–37.
Sadat, R.S., Huang, J., Bin-Shafique, S., Rezaeimalek, S., 2018. Study of the behavior of mechanically stabilized earth (MSE) walls subjected to differential settlements. Geotext. Geomembranes 46 (1), 77–90.
Skinner, G.D., Rowe, R.K., 2003. Design and behavior of geosynthetic reinforced soil wall constructed on yielding foundation. Geosynth. Int. 18 (5), 304–321.
Skinner, G.D., Rowe, R.K., 2005a. A novel approach to estimating the bearing capacity stability of geosynthetic reinforced retaining walls constructed on a yielding foundation. Can. Geotech. J. 42 (3), 763–779.
Skinner, G.D., Rowe, R.K., 2005b. Design and behavior of geosynthetic reinforced retaining wall and bridge abutment constructed on a yielding foundation. Geotext. Geomembranes 23 (3), 234–260.
Stulgis, R.P., Soydemir, C., Telgener, R.J., Hewitt, R.D., 1996. Use of geosynthetics in 'piggyback landfills': a case study. Geotext. Geomembranes 14 (7–8), 341–364.
Talebi, M., Meehan, C.L., Leshchinsky, D., 2017. Applied bearing pressure beneath a reinforced soil foundation used in a geosynthetic reinforced soil integrated bridge system. Geotext. Geomembranes 45 (6), 580–591.
Tin, N., Bergado, D.T., Voottipruex, P., Tanchaisawat, T., 2011. Modification of K-stiffness methods for MSE structures on soft ground. Geosynth. Int. 10 (10), 200–214.
Viswanadham, B.V.S., Konig, D., 2004. Studies on scaling and instrumentation of a geogrid. Geotext. Geomembranes 22 (5), 307–328.
Viswanadham, B., Muthukumaran, A., 2007. Influence of geogrid layer on the integrity of compacted clay liners of landfills. Soils Found. 47 (3), 517–532.
Viswanadham, B.V.S., Konig, D., 2009. Centrifuge modeling of geotextile-reinforced slopes subjected to differential settlements. Geotext. Geomembranes 27 (2), 77–88.
Wu, J.T.H., 1991. Measuring inherent load-extension properties of geotextiles for design of reinforced structures. Geotech. Test J. 14 (2), 157–165.
Wu, J.T.H., Lee, K.Z.Z., Helwany, S., Ketchart, K., 2006. Design and Construction Guidelines for Geosynthetic-Reinforced Soil Bridge Abutments with a Flexible Facing. National Cooperative Highway Research Program, Washington D.C Report 556.
Yang, K.H., Zornberg, J.G., Liu, C.N., Lin, H.D., 2012. Stress distribution and development within geosynthetic-reinforced soil slopes. Geosynth. Int. 19 (1), 1–17.
Zheng, Y., Fox, P.J., 2017. Numerical investigation of the geosynthetic reinforced soil-integrated bridge system under static loading. J. Geotech. Geoenviron. Eng. ASCE 143 (6) 04017008.
Zornberg, J.G., Arriaga, F., 2003. Strain distribution within geosynthetic-reinforced slopes. J. Geotech. Geoenviron. Eng. ASCE 129 (1), 32–45.